

# The He I $\lambda 10830$ Å line as a probe of winds and accretion in young stars in Lupus and Upper Scorpius <sup>★</sup>

J. Erkal<sup>1,2</sup>, C.F. Manara<sup>1</sup>, P.C. Schneider<sup>3</sup>, M. Vincenzi<sup>4</sup>, B. Nisini<sup>5</sup>, D. Coffey<sup>2</sup>, J.M. Alcalá<sup>6</sup>, D. Fedele<sup>7</sup>, S. Antonucci<sup>5</sup>

<sup>1</sup> European Southern Observatory, Karl-Schwarzschild-Strasse 2, 85748 Garching bei München, Germany  
e-mail: jessica.erkal@eso.org

<sup>2</sup> School of Physics, University College Dublin, Belfield, Dublin 4, Ireland

<sup>3</sup> Hamburger Sternwarte, Gojenbergsweg 112, 21029, Hamburg, Germany

<sup>4</sup> Department of Physics, Duke University, Durham, NC 27708, USA

<sup>5</sup> INAF-Osservatorio Astronomico di Roma, Via di Frascati 33, 00078 Monte Porzio Catone, Italy

<sup>6</sup> INAF-Osservatorio Astronomico di Capodimonte, via Moiariello 16, 80131 Napoli, Italy

<sup>7</sup> INAF-Osservatorio Astrofisico di Arcetri, Largo Enrico Fermi 5, 50125, Firenze, Italy

August 1, 2022

## ABSTRACT

**Context.** The He I  $\lambda 10830$  Å line is a high excitation line which allows us to probe the material in the innermost regions of protostellar disks, and to trace both accreting and outflowing material simultaneously.

**Aims.** We use X-Shooter observations of a sample of 107 young stars in the Lupus (1–3 Myr) and Upper Scorpius (5–10 Myr) star-forming regions to search for correlations between the line properties, as well as the disk inclination and accretion luminosity.

**Methods.** We identified eight distinct profile types in the sample. We fitted Gaussian curves to the absorption and/or emission features in the line to measure the maximum velocities traced in absorption, the full-width half-maximum (FWHM) of the line features, and the Gaussian area of the features.

**Results.** We compare the proportion of each profile type in our sample to previous studies in Taurus. We find significant variations between Taurus and Lupus in the proportion of P Cygni and inverse P Cygni profiles, and between Lupus and Upper Scorpius in the number of emission-only and combination profile types. We examine the emission-only profiles in our sample individually and find that most sources (nine out of 12) with emission-only profiles are associated with known jets. When examining the absorption features, we find that the blue-shifted absorption features appear less blue-shifted at disk inclinations close to edge-on, which is in line with past works, but no such trend with inclination is observed in the sources with only red-shifted features. Additionally, we do not see a strong correlation between the FWHM and inclination. Higher accretion rates were observed in sources with strong blue-shifted features which, along with the changes in the proportions of each profile type observed in the two regions, indicates that younger sources may drive stronger jets or winds.

**Conclusions.** Overall, we observe variations in the proportion of each He I  $\lambda 10830$  Å profile type and in the line properties which indicates an evolution of accretion and ejection signatures over time, and with source properties. These results confirm past works and models of the He I  $\lambda 10830$  Å line, but for a larger sample and for multiple star-forming regions. This work highlights the power of the He I  $\lambda 10830$  Å line as a probe of the gas in the innermost regions of the disk.

**Key words.** Stars: pre-main sequence – stars: formation – protoplanetary disks – accretion, accretion disks

## 1. Introduction

From the earliest stages of star formation, jets and outflows are commonly observed from young stars (Frank et al. 2014). At the same time, accretion occurs as material flows radially inwards through the disk onto the star (Hartmann et al. 2016). The interplay between these two processes is relevant for the final stellar mass and for the removal of disk mass, which impacts the material available for planet formation (Manara et al. 2018). However, the connection between accretion and ejection is not fully understood (e.g. Pascucci et al. 2022; Manara et al. 2022).

Accretion occurs as material is transported through the disk. When the material reaches the disk truncation radius ( $R_t \simeq 3\text{--}7 R_\star$ ), it falls along magnetic field lines in accretion flows onto the star (Hartmann et al. 2016). As the material falls onto the star, accretion shocks lead to excess emission in ultraviolet and optical wavelengths, which causes photospheric absorption features in the spectra to appear shallower (i.e. veiling). Veiling also occurs at infrared (IR) wavelengths (e.g. Folha & Emerson 1999, Fischer et al. 2011).

Magnetic fields in the disk are likely responsible for the launching and collimation of jets and outflows seen in young stars (Pudritz & Ray 2019). The highly collimated, high velocity jets are generally observed to have a knotty structure, suggesting that material is not ejected at a constant rate. If these jets are accretion powered, the knotty structure points to variable accretion with periods of high accretion in accretion bursts and a smaller

<sup>★</sup> This work is based on observations made with ESO telescopes at the La Silla Paranal Observatory under programme ID 084.C-0269, 084.C-1095, 086.C-0173, 087.C-0244, 089.C-0143, 085.C-0238, 085.C-0764, 089.C-0840, 090.C-0253, 093.C-0658, 094.C-0913, 095.C-0134, 095.C-0378, 097.C-0349, 097.C-0378, and 0101.C-0866, and archive data of programmes 085.C-0764 and 093.C-0506.

contribution made by a lower constant accretion rate (e.g. Arce et al. 2007; Vorobyov et al. 2018). Often surrounding the high-velocity jet is a slower wind ejected directly from the disk (photoevaporative winds or magnetohydrodynamic (MHD) winds, for example, Pudritz & Norman 1983; Ercolano & Pascucci 2017). In younger Class 0/I sources, these outflows may also contain entrained material swept up by the jet (e.g. Zhang et al. 2019). These jets and outflows can be traced back to the star-disk plane, and they appear to be launched through MHD processes from the inner regions of the disk (Blandford & Payne 1982; Pudritz & Norman 1983), though the exact launching mechanism is not yet known (Ferreira et al. 2006). However, it is still not clear which mechanism dominates the mass removal throughout the evolution of the protostar, as photoevaporative winds (see e.g. Ercolano & Pascucci 2017) may also drive the wider outflows. Photoevaporation is important for disk dispersal, but it does not contribute to the removal of angular momentum. The launching of a magnetically driven jet from the disk is believed to play a role in angular momentum removal, which drives accretion onto the star (Ercolano & Pascucci 2017; Bai 2016), thus highlighting the connection between accretion and ejection in young stellar systems. This is further supported by the correlation between mass loss rates and the disk accretion rate ( $\dot{M}_{\text{out}}/\dot{M}_{\text{acc}} \approx 10\%$ , e.g. Cabrit et al. 1990, Hartigan et al. 1995, Nisini et al. 2018). On the contrary, through viscous evolution, angular momentum is transported through the disk (Hartmann et al. 1998), rather than being removed via an outflow, and so it is not possible to find a connection between accretion and ejection in this scenario. An exception to this is in the case of X-winds which are launched near the corotation radius, where the magnetosphere truncates the disk (see e.g. Shu et al. 1994). Many of these winds and outflows are traced by forbidden emission lines (e.g. [O I], [S II], [Fe II]; see e.g. Pascucci et al. 2022) within which a high-velocity component (HVC) and low-velocity component (LVC) are often detected. The HVC is attributed to the high-velocity jets, while the LVC is linked to the slower disk winds which show correlations with the accretion luminosity (e.g. in the [O I]  $\lambda 6300$  Å line). However, to understand the true nature of the connection between accretion and ejection in young stars, we must find a way to examine the innermost regions of the disk.

High excitation lines have been used as a probe of the inner regions of the disk, since their formation is confined to high temperature regions or near ionizing radiation (Beristain et al. 2001; Edwards et al. 2003), in the inner au (Edwards 2009). One such line is the He I  $\lambda 10830$  Å line. With high excitation and a metastable lower level, this line is particularly sensitive to sub-continuum absorption providing a way to probe both accretion and ejection in the inner disk regions simultaneously. Red-shifted absorption in this line traces accreting material, travelling near free-fall velocity onto the star. The red-shifted absorption creates the inverse P Cygni profile and is generally seen at velocities between 0 to  $350 \text{ km s}^{-1}$  (Fischer et al. 2008). Red-shifted absorption was identified as a good tracer of accretion as Edwards et al. (2006) noted that even though this feature is often observed at Classical T Tauri stars (CTTSs) with ongoing accretion, no such feature is observed at non-accreting Weak-line T Tauri stars (WTTSs; see Figure E.1 for He I  $\lambda 10830$  Å line profiles in non-accreting Class III sources). However, the absence of red-shifted absorption may point to the presence of emission from a wind which fills the absorption feature, or high veiling of the star. Thanathibodee et al. (2022), for example, used the He I  $\lambda 10830$  Å line to study young stars previously thought to be non-accretors.

Winds are traced by blue-shifted absorption which traces outflowing material, and can be linked to a stellar wind or disk wind depending on the absorption profile. Wide blue-shifted absorption features are formed by a radially expanding stellar wind which is traced up to several hundred  $\text{km s}^{-1}$ , whereas narrow low-velocity absorption features indicate the presence of a disk wind, where only a small range of velocities in the wind are intercepted along the line of sight to the star (Edwards et al. 2006; Edwards 2009). Emission may also trace a polar wind at the star if the star is highly inclined (Kwan et al. 2007). The He I  $\lambda 10830$  Å line likely traces a stellar wind because narrow absorption features in the line, characteristic of disk winds, are observed less frequently than stellar wind signatures (Edwards et al. 2006; Kwan et al. 2007). Nonetheless, both a disk wind and stellar wind could coexist at these stars, both removing mass and angular momentum from the system. Red-shifted absorption, tracing accreting gas, was observed more frequently in the He I line than in other lines (e.g. Pa $\gamma$ ) where veiling likely prevents the detection of this feature as shown by Fischer et al. (2008).

However, past studies have only dealt with small samples ( $n \approx 30$ ) of stars of the same age, i.e. all situated in the same star forming region, e.g. Taurus (1-3 Myr, Krolikowski et al. 2021). Observing larger samples of stars from different star forming regions is key to establishing a connection between the accretion and ejection in these sources, for various stages of evolution.

In this paper we present the analysis of a sample of over 100 young stars in the Lupus (1–3 Myr, Comerón 2008; Luhman 2020) and Upper Scorpius (5–10 Myr, Pecaute et al. 2012; Luhman 2022) star forming regions. We observe the He I  $\lambda 10830$  Å line at higher resolution and for a larger sample size than past works, providing an opportunity to identify statistically significant trends in the data. The He I  $\lambda 10830$  Å line is examined for each star and categorised into profile types to search for trends with respect to age, stellar properties and accretion properties.

The paper is organised as follows. The sample, observations and data reduction are presented in Section 2. In Section 3 we describe the method used for identifying the He I  $\lambda 10830$  Å profile types (Section 3.1). Here we also describe each profile type identified in our sample (Section 3.2). In Section 4 we present statistics on profile type occurrences in each region and measured absorption velocities. We discuss our results in Section 5, focusing in particular on observed trends in velocities, and dependences on source inclination and accretion properties. Our main conclusions are summarised in Section 6.

## 2. Sample, observations, and data reduction

### 2.1. Sample

Our sample consists of a total of 117 young stellar objects - 82 Class II sources are located in the Lupus star forming region ( $d \approx 160$  pc; Alcalá et al. 2014, 2017) and a further 35 sources in Upper Scorpius ( $d \approx 145$  pc; Manara et al. 2020). The Lupus sample is younger (1 – 3 Myr; Comerón 2008) compared to the Upper Scorpius sample (5 – 10 Myr; Luhman & Mamajek 2012), allowing us to investigate the evolution of the He I  $\lambda 10830$  Å profile for different ages. The targets in our sample have spectral types between K0 and M8.5, with stellar masses in the range of  $M_* \approx 0.1 - 1.6 M_{\odot}$  (see Figures 1 and 2), allowing us to investigate the properties of the He I  $\lambda 10830$  Å line in relation to varying stellar properties such as spectral type, accretion luminosity, among others. We include information on the spectral types, disk inclination, and accretion properties for the individual targets in

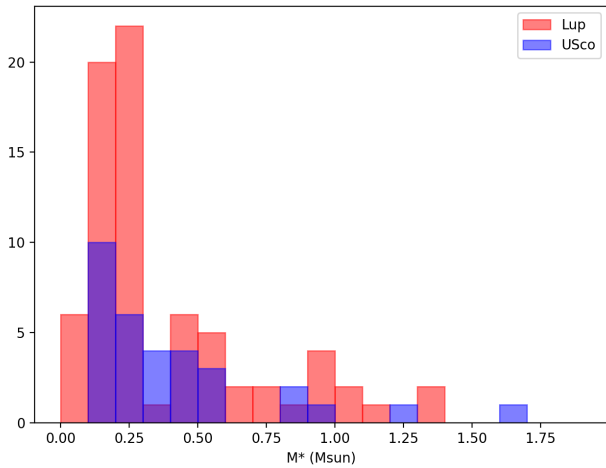


Fig. 1: Stellar masses observed in both the Lupus (red) and Upper Scorpius (blue) regions.

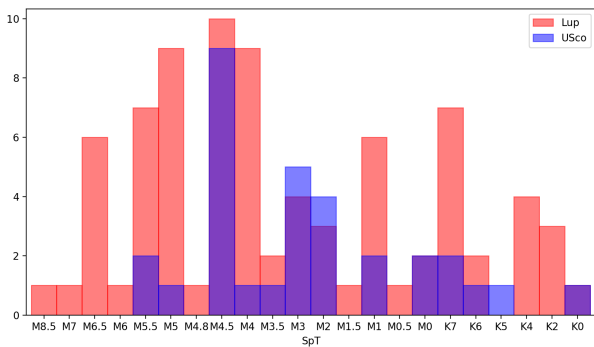


Fig. 2: Spectral types of the central star observed in both the Lupus (red) and Upper Scorpius (blue) regions.

Tables A.1 and A.2, however the sample is described in depth in Alcalá et al. (2014, 2017) and Manara et al. (2020).

## 2.2. Observations

All the observations included in this work have been obtained with the ESO/VLT X-Shooter spectrograph (Vernet et al. 2011). This medium-resolution and high-sensitivity instrument simultaneously covers the wavelength range between  $\sim 300$  nm and  $\sim 2500$  nm. The spectra are divided in three arms which cover three different wavelength ranges. The helium line analysed here is located in the NIR arm, with resolution  $R \sim 10500$ -5300 depending on the slit width. The spectra used in this analysis have been reduced with the procedure described by Alcalá et al. (2014), and the observational details are listed in Alcalá et al. (2014, 2017) and Manara et al. (2020) depending on the targets, as discussed in the following section.

## 2.3. Data reduction

The data were initially reduced with the X-Shooter pipeline (Modigliani et al. 2010) using the ESO Reflex workflow. This process is described in detail in previous works where the same data reduction steps are taken, for example Alcalá et al. (2017) and Manara et al. (2020). The telluric correction procedures for both regions are also described in these papers. Telluric correction for the Lupus sample was performed using two separate

methods on the NIR and VIS arms (see Appendix A in Alcalá et al. 2014, for detail). The telluric correction for Upper Sco sources was carried out using molecfit (Smette et al. 2015; Kausch et al. 2015) as described by Manara et al. (2020). Radial velocity (from Frasca et al. 2017; Manara et al. 2020) and heliocentric velocity corrections are applied to both the NIR and VIS spectra. To correct for wavelength shifts between the two arms, we used a 1D Gaussian fit to measure the centroid of the Lithium 670.78 nm absorption line and the Pa $\delta$  1004.94 nm line (observed in both the NIR and VIS spectra). We first fitted the Li 670.78 nm line with a 1D Gaussian, finding median Lithium shifts of  $\sim -0.5$  km s $^{-1}$  and  $-0.4$  km s $^{-1}$  for Lupus and Upper Sco. The Li shift is applied to both NIR and VIS spectra, such that the lithium line is centred on 0 km s $^{-1}$ . We then corrected for wavelength shifts between the NIR and VIS spectra using the Pa $\delta$  line present in both arms. We found median Pa $\delta$  shifts of  $\sim 9$  km s $^{-1}$  and  $-2.96$  km s $^{-1}$  for the Lupus and Upper Sco samples (respectively), which is then applied to the NIR spectrum. In a few cases where the signal-to-noise was too low for the lines to be properly fitted, we applied the median shifts listed above to these spectra. We find typical  $1\sigma$  errors on the Li and Pa $\delta$  velocity corrections of 2.96 km s $^{-1}$  and 2.24 km s $^{-1}$ , respectively. Adding these in quadrature, the combined error due to the velocity corrections is 3.7 km s $^{-1}$  and thus do not introduce large uncertainties in the observed maximum velocities in the He I  $\lambda 10830$  Å line (see Section 4). We describe the process of aligning the NIR and VIS spectra in more detail in Appendix B.

## 2.4. Ancillary data

We have gathered further information on our sample for the analyses presented later in this paper. We use the stellar mass and luminosities, and accretion properties ( $\dot{M}_{\text{acc}}$  and  $L_{\text{acc}}$ ) from Alcalá et al. (2019) for the Lupus sources, and from Manara et al. (2020) for Upper Scorpius sources, with distances for the individual sources from DR2 of the Gaia Collaboration (2018). The disk inclinations are known for 103 (88%) of the 117 sources in our sample (85% in Lupus, 94% in Upper Sco) and were measured from ALMA continuum observations for the Lupus sample by Tazzari et al. (2017), Ansdell et al. (2018), and Yen et al. (2018) and for Upper Scorpius by Barenfeld et al. (2017). We note that these are measurements of the outer disk inclinations, whereas the He I  $\lambda 10830$  Å line traces gas close to the star. Since it is possible that there is a misalignment between the inner and outer disk (e.g. Bohn et al. 2022) this possible issue will be considered when the results are analysed.

## 3. Data analysis

### 3.1. Automatic determination of line profile types

We examined the He I  $\lambda 10830$  Å line profile in all of our targets using *scipy* routines (Virtanen et al. 2020) in Python 3. We located the positions of all minima and maxima in the spectra between  $\pm 400$  km s $^{-1}$  with the *find\_peaks* routine, considering only those extrema with absolute intensities larger than twice the rms to avoid measuring noise. Using the location (in velocity) of the extrema and their height relative to the continuum (i.e. absorption or emission), we can distinguish between various profile types, described in further detail in Section 3.2. We used this initial information on the extrema and profile types to provide initial guesses on the peak parameters (amplitude, centroid in km s $^{-1}$  and standard deviation in km s $^{-1}$ ) for Gaussian fitting. Depending on the profile type, between one to four 1D

Gaussians were fitted to the He I  $\lambda 10830$  Å profiles using *scipy*'s *curve\_fit* routine, by adding the suitable number of 1D Gaussian functions defined as:

$$f(x) = ae^{-\frac{1}{2}\left(\frac{x-\mu}{\sigma}\right)^2} \quad (1)$$

where  $a$  is the amplitude,  $\mu$  is the centroid and  $\sigma$  is the standard deviation of the Gaussian peak.

We measured the  $\chi^2$  to identify poor fits (i.e. fits with  $\chi^2 > 0.5$ ) which we fitted again manually using new initial guesses for the peak parameters and profile type. We also visually checked each fit to ensure the profile is well-fitted (see Figures C.1, C.2 and D.1 for each fitted profile). Out of the 82 sources in Lupus, 30 sources could not be automatically fitted and required manual inputs for a good fit. These profiles generally were categorised into the low-velocity absorption or miscellaneous profile types. Additionally, some of the profile types for these sources were identified incorrectly, therefore they required manual inputs and bounds to accurately fit the He I  $\lambda 10830$  Å line profile. These sources are listed in Table 1. Only one He I  $\lambda 10830$  Å profile in Lupus (2MASSJ16085373-3914367) could not be fitted due to low signal-to-noise and/or bad pixels. In Upper Scorpius, all sources could be fitted using a combination of 1D Gaussians, with 15 sources requiring manual inputs to be accurately fitted - these are listed in Table 2.

### 3.2. He I $\lambda 10830$ Å line profiles

We identified eight distinct profile types in the data. The conceptual line profiles are presented in the left column of Figure 3 and were created by adding between one to four one-dimensional Gaussians to the continuum, which is set at zero for all profiles. The profile types are as follows:

- Pure emission profiles are characterised by a single peak in emission. There are no sub-continuum absorption features present in these profiles.
- Pure absorption profiles are characterised by a single absorption feature. There are no other absorption features, or emission observed in these profiles.
- P-Cygni profiles are characterised by the presence of a sub-continuum blue-shifted absorption feature, and emission centred near  $0 \text{ km s}^{-1}$  or slightly red-shifted. There is no red-shifted absorption feature observed.
- Inverse P-Cygni profiles are characterised by the presence of a sub-continuum red-shifted absorption feature, and emission centred at low velocities. There is no blue-shifted absorption feature observed. The red-shifted absorption feature is generally wider than the absorption observed in P-Cygni profile types.
- Combination profiles are characterised by the presence of two absorption features, one is red-shifted and the other is blue-shifted, and emission centred near  $\sim 0 \text{ km s}^{-1}$ . These profiles are a combination of the P-Cygni and Inverse P-Cygni profiles, with similar profile characteristics in both the blue- and red-shifted absorption features.
- Low velocity absorption (LVA) profiles are characterised by an overlapping emission feature and absorption feature, both centred near  $\sim 0 \text{ km s}^{-1}$ . These profiles are distinguished from a P-Cygni or Inverse P-Cygni profile due to the presence of emission on both sides of the absorption feature.
- Double absorption (DA) profiles are characterised by the presence of two sub-continuum absorption features generally within  $\pm 200 \text{ km s}^{-1}$ . There is no emission observed in these profiles.

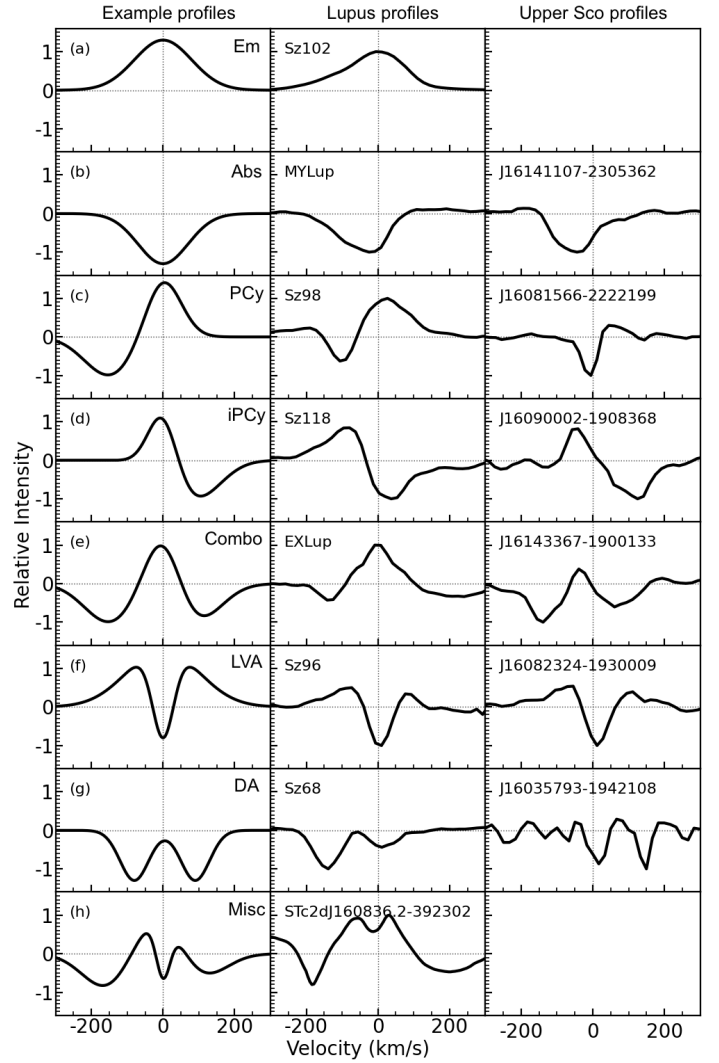


Fig. 3: Theoretical profile types and example He I  $\lambda 10830$  Å profiles observed in our data. The left column shows the theoretical profiles for the eight profile types described in Section 3.2. The middle and right columns show examples of each profile type in the Lupus and Upper Scorpius samples, respectively. The flux has been normalised to the continuum level in each source, and rescaled between  $\pm 1$  for plotting. The grey horizontal line marks the continuum level at 0, while the vertical grey line denotes  $0 \text{ km s}^{-1}$ . We observe no pure emission or miscellaneous profile types in the Upper Scorpius sample.

- Miscellaneous profile types are also observed in the data and are those which cannot be accurately described by any of the above profile types.

Figure 4 shows a sketch of an example protostellar system with accretion flows along which material moves from the inner disk onto the star, and with a jet and disk wind present. The dark grey dashed arrows show different viewing angles which result in different He I  $\lambda 10830$  Å line profiles. In the scenario where the source is viewed along a line-of-sight passing through an accretion flow, a red-shifted sub-continuum absorption feature is observed in the line profile. Emission-only profiles may be observed if the source is sub-luminous and/or close to edge-on resulting in the observation of only jet/wind emission. Close to face-on, the emission is absorbed by the higher velocity com-

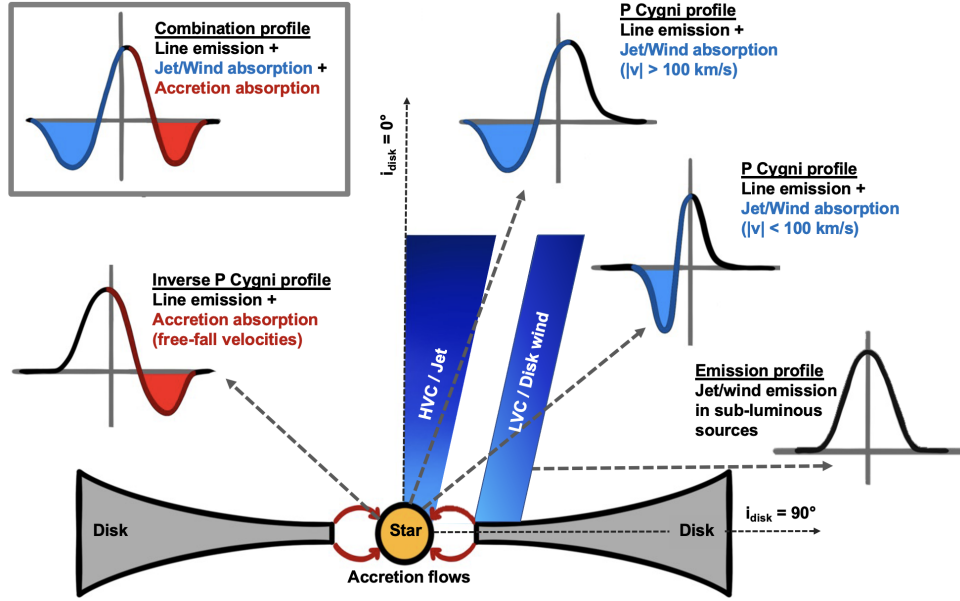


Fig. 4: Schematic diagram of various He I  $\lambda 10830$  Å line profiles observed along different line of sights (grey dashed arrows) depending on source inclination (based on McJunkin et al. (2014); Xu et al. (2021)).

ponents of a jet/outflow which results in wider blue-shifted absorption profiles at larger velocities. Meanwhile, for closer to edge-on observations, the observer's line-of-sight passes through the low velocity parts of the outflow (possibly a disk wind), thus producing a narrower absorption feature at less blue-shifted velocities. In some cases, the line-of-sight may pass through both a jet or wind, and an accretion flow resulting in two absorption features in the line profile (see inset in Figure 4). In this figure, we do not include absorption-only profiles, double absorption profiles or low-velocity absorption profiles since they occur less frequently in our sample.

## 4. Results

### 4.1. Profile appearance statistics

We fitted the He I  $\lambda 10830$  Å profiles in the Lupus and Upper Scorpius samples as described in Section 3.1. Figure 5 shows the percentage of targets characterised into each profile type for both regions. Information on the profile type and centroid velocities of the emission and absorption features are listed in Tables 1 - 2. We also compare the proportion of profile types observed in our sample to those of a sample of 38 targets located in the Taurus star forming region from Edwards et al. (2006). In Lupus (middle, Figure 5) we find that the most common profile type are inverse P Cygni profiles (27 of the 82 targets, i.e. 33%), followed by combination type profiles (13 targets or 16%). However in Upper Scorpius (right, Figure 5) the combination profiles (11 of the 35 targets, 31%) and inverse P Cygni profiles are the most common types (12 targets, 34%), followed by P Cygni profiles (five targets, 14%). In Upper Scorpius we do not observe any pure emission profiles. In Taurus, a large portion of the He I  $\lambda 10830$  Å profiles show a P Cygni profile (19 of 38 targets, 50%), followed by the combination profile type (15 targets, 39%). There are no single absorption or double absorption profiles observed in the Taurus sample. We stress that the Taurus sample in Edwards et al. (2006) (38 objects in total) is much smaller than our sample in Lupus (82 objects), but is comparable

in size to our sample in Upper Sco (35 objects). The Taurus sample however is predominantly K7 and M0 type stars, compared to a larger range of spectral types from K0 to M8.5 in our sample. We believe these differences may contribute to the varying proportions of each profile type observed in each region. Further, we note that the resolution of the Taurus observations is higher than the resolution of our observations. The resolution with NIRSPEC used for the Taurus sample is  $R \approx 25000$  (Edwards et al. 2006), while the X-Shooter resolution is  $\approx 10000$ . In velocity, this is roughly equal to  $12 \text{ km s}^{-1}$  and  $30 \text{ km s}^{-1}$  for NIRSPEC and X-Shooter respectively. However, the widths of the features in our sample are typically larger than this resolution, thus we do not believe these variations are due to an instrumental effect.

### 4.2. Absorption velocity properties

In Figure 6 we present scatter plots and histograms of the maximum absorption velocities for the red- and blue-shifted absorption features. The maximum absorption velocity is the highest velocity observed in the absorption feature, i.e. the most blue-shifted velocity in absorption for blue absorption features and the most red-shifted velocity in red absorption features. We calculated the maximum velocities using the fitted Gaussian velocity centroids ( $\mu$  or  $v_{cen}$ ) and standard deviations ( $\sigma$ ) i.e.  $v_{max} = v_{cen} \pm 3\sigma$ . We display the typical  $3\sigma$  fitting errors for the red- and blue-shifted maximum velocities in panels (b) and (d), respectively, which are obtained from the covariance matrix of the Gaussian fit from *scipy curve\_fit*.

The majority of red-shifted velocities appear to cluster at velocities of  $\approx 200 \text{ km s}^{-1}$ , and increase with stellar mass such that they are compatible with free-fall velocities for stellar radii between  $R_{\star} = 1$  and  $2 R_{\odot}$ , assuming the radius for magnetospheric accretion is equal to  $5 R_{\star}$  (Hartmann et al. 2016). The free-fall velocities are calculated with the following simplified equation from Hartmann et al. (2016):

$$v_{ff} = \left( \frac{2GM_{\star}}{R_{\star}} \right)^{1/2} \left( 1 - \frac{R_{\star}}{R_M} \right)^{1/2} \approx 280 M_{0.5}^{1/2} R_2^{-1/2} \text{ km s}^{-1}, \quad (2)$$

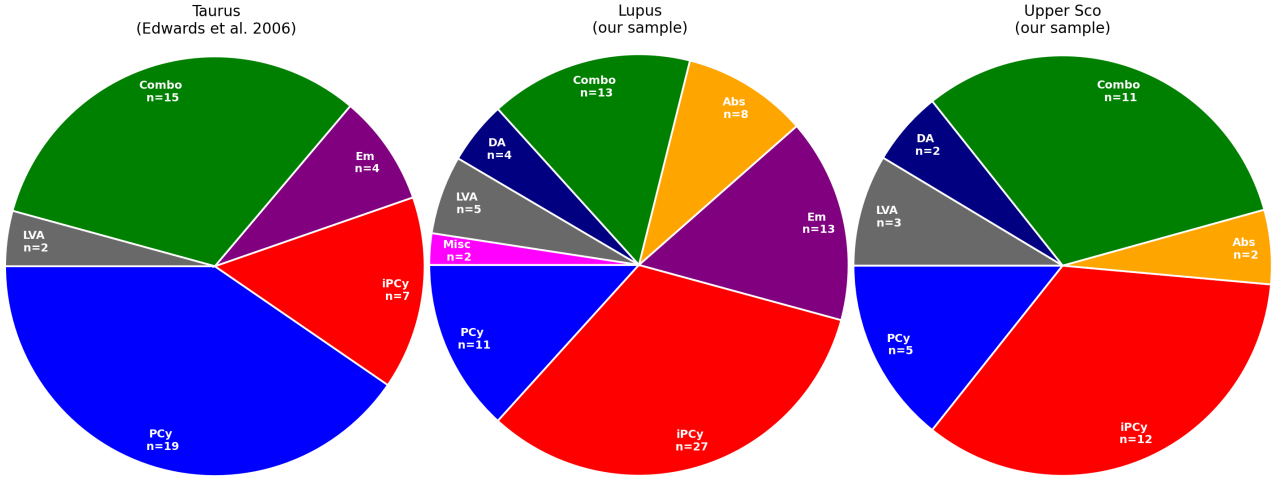


Fig. 5: Pie charts showing the proportions of each profile type identified in our sample of 82 sources in Lupus and 35 sources in Upper Scorpius, middle and right respectively. We compare the proportion of profile types observed in our sample to those of a sample of 38 targets located in the Taurus star forming region from Edwards et al. (2006). The colours of the wedges in each pie chart represent each profile type - blue P Cygni profiles; red inverse P Cygni profiles; purple pure emission profiles; orange absorption-only profiles; green combination profiles; navy blue double absorption profiles; grey low velocity absorption profiles and pink miscellaneous profiles.

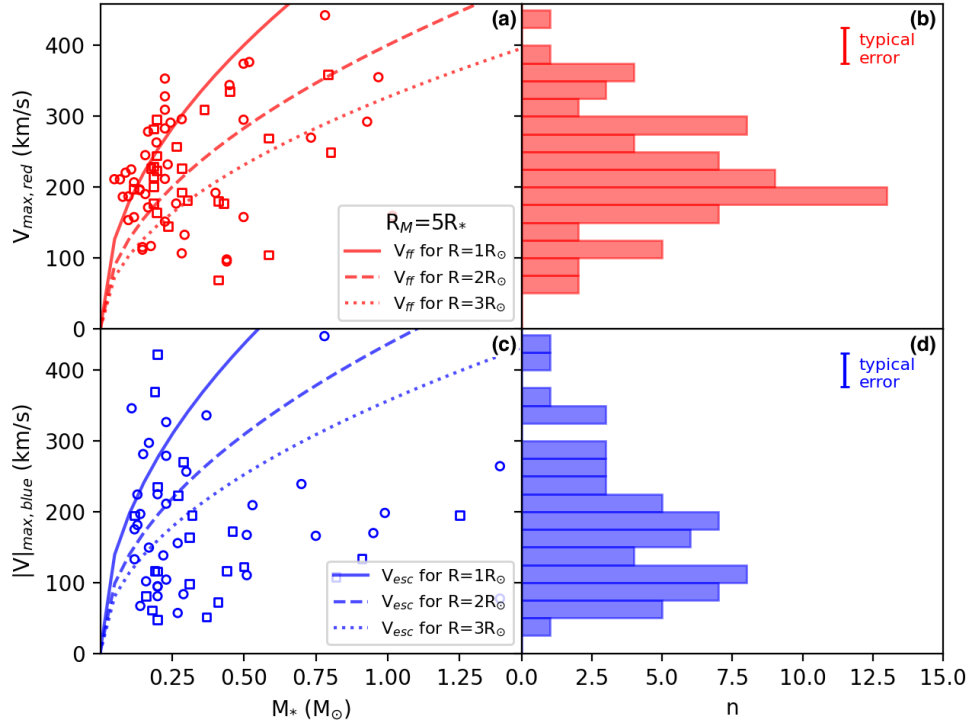


Fig. 6: Maximum velocities of the red- and blue-shifted absorption features (panels (a) and (c), respectively) observed in the He I  $\lambda 10830$  Å profiles. Panels (a) and (c) show scatter plots of the Lupus absorption velocities with circles, and Upper Scorpius velocities with squares. The solid, dashed and dotted lines are the free-fall velocities (panel (a)) and escape velocities (panel (c)) for stellar radii  $R_* = 1, 2, 3 R_\odot$ , respectively. Panels (b) and (d) show histograms of the maximum absorption velocities for both regions in  $10 \text{ km s}^{-1}$  velocity bins.

where  $G$  is the universal gravitational constant,  $R_M$  is the magnetospheric radius from which material falls inwards along accretion flows, and  $M_{0.5}$  and  $R_2$  are the stellar mass and radius in units of  $0.5 M_\odot$  and  $2 R_\odot$ . The stellar radii for each source in our sample were calculated using the stellar luminosity and effective temperatures found in Alcalá et al. (2019) for the Lupus sample and Manara et al. (2020) for the Upper Scorpius sample.

The typical  $R_*$  for our targets is  $\sim 1.3 R_\odot$  for Lupus and  $\sim 1.05 R_\odot$  for Upper Scorpius. We calculated the radius at which the infalling material reaches free-fall velocities ( $R_{\text{ff}}$ ) by rearranging Equation 1 in Fischer et al. (2008) so that:

$$v_{\text{ff}} = v_{\text{esc}} \left( \frac{R_*}{R_{\text{ff}}} - \frac{R_*}{R_M} \right)^{1/2} \quad (3)$$



becomes

$$R_{\text{ff}} = R_{\star} v_{\text{esc}} \left( \frac{R_M v_{\text{esc}}}{1 + R_M v_{\text{ff}}^2} \right) \quad (4)$$

where  $R_M$  is set to  $5 R_{\star}$  following the assumptions of Hartmann et al. (2016) (see above) and where  $v_{\text{esc}}$  is the escape velocity defined as:

$$v_{\text{esc}} = \sqrt{2GM_{\star}/R_{\star}} \quad (5)$$

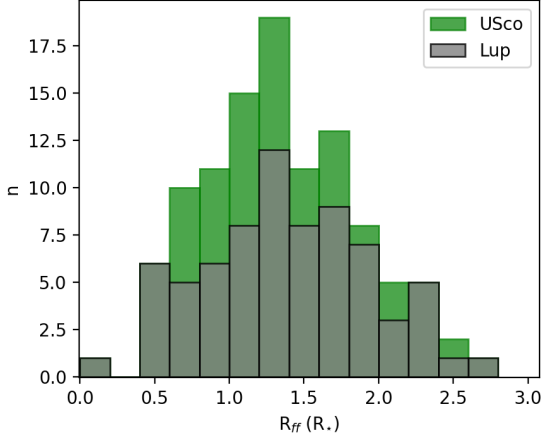


Fig. 7: Stacked histogram of the radius in the disk at which the material reaches free-fall velocities. The total value of each bin accounts for sources in both Lupus and Upper Scorpius.

For sources in Lupus,  $R_{\text{ff}}$  is approximately  $1.6 R_{\star}$  while in Upper Scorpius  $R_{\text{ff}} \sim 1.3 R_{\star}$  (see Figure 7). This typically corresponds to  $\sim 1.4\text{--}2 R_{\odot}$  in line with the curves in Figure 6 (see Section 5.2 for further discussion).

The blue-shifted velocities in our sample tend to appear at lower velocities than their red-shifted counterparts, but are not as confined to specific velocities. Further, they generally reach escape velocities from the star. We note that the escape velocities calculated for our sample are from the star, and that if the material is launched in a disk wind, the escape velocities from the disk are smaller.

For each source in Lupus and Upper Scorpius, in Figure 8, we plot histograms of the difference between the observed maximum red-shifted velocities and free-fall velocity, and between the maximum blue-shifted velocities and escape velocity from the star. The red-shifted maximum velocities appear to be similar to the free-fall velocities, with a mean value of  $-80.6 \text{ km s}^{-1}$ . Meanwhile, the blue-shifted velocities are generally larger than the escape velocity with many of the values of  $v_{\text{max}} - v_{\text{esc}}$  between  $100\text{--}200 \text{ km s}^{-1}$  (and a mean value of  $157 \text{ km s}^{-1}$ ), but their distribution is flatter spanning a large value of mostly positive velocity differences.

In Figures 9 and 10 we present the maximum absorption velocities and the FWHM of the absorption features with respect to the inclination of the source for both the Lupus and Upper Scorpius regions. In Figure 9, we observe the maximum blue-shifted velocity trending to lower velocities at higher inclinations (panel (a)). This is not seen in their red-shifted counterparts, as the red-shifted velocities remain  $\geq 150 \text{ km s}^{-1}$  (panel (b)), even for highly inclined targets. In combination profiles (downward

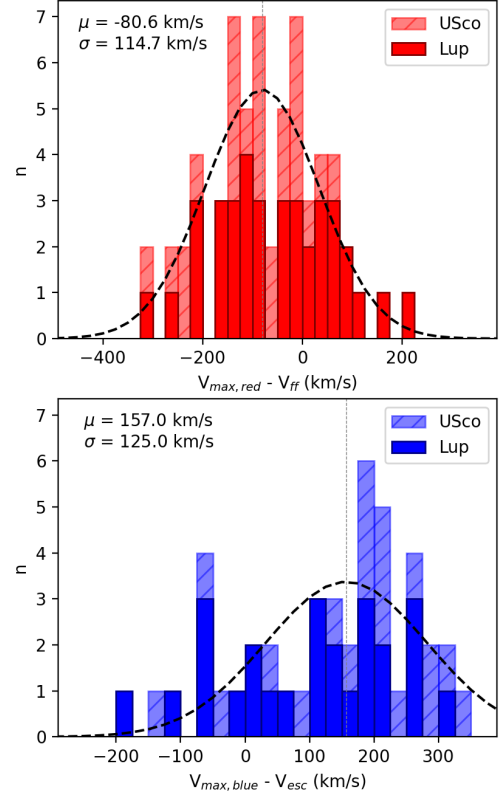


Fig. 8: Stacked histograms of the observed red-shifted maximum velocities compared to the free-fall velocities (top), and blue-shifted maximum velocities compared to the escape velocity (bottom), where the total value in each bin is the number of sources in both Lupus and Upper Scorpius. The dashed black line in each panel shows the Gaussian distributions fitted to the histogram data, with the centroid ( $\mu$ ) and standard deviation ( $\sigma$ ) of this fit noted in the top left corner.

triangles), most blue absorption features appear to have a maximum velocity of  $\approx 150 - 200 \text{ km s}^{-1}$ , while a second cluster of velocities closer to  $350 \text{ km s}^{-1}$  which are generally the red-shifted absorption feature for these profiles. Given that the velocities for combination profiles appear across all inclinations, we believe that they are not due only to a particular viewing angle. Red-shifted absorption features tend to occur at higher velocities than the blue absorption features, and they also appear generally wider (see Figure 10). This may suggest that we can observe a wider range of accretion velocities than velocities in the wind, hinting at a dependence on the source inclination. Red-shifted velocities, however, are not related to the source inclination, like the blue-shifted features as evident in the p-values displayed in each panel. In Figure 10 we find that the red-shifted absorption features are wider (typical FWHM  $\approx 100 \text{ km s}^{-1}$ ) than the blue-shifted features (typical FWHM  $\approx 50\text{--}100 \text{ km s}^{-1}$ ). This is noticeable even in the combination profiles (downwards triangles). However, we do not find a correlation between the width of the absorption features and the source inclination.

## 5. Discussion

In the following sections we discuss the results presented in Section 4. We begin by focusing on the He I  $\lambda 10830 \text{ \AA}$  profiles with pure emission profiles and the presence of known jets in these sources. Following this, we examine the profiles with absorption

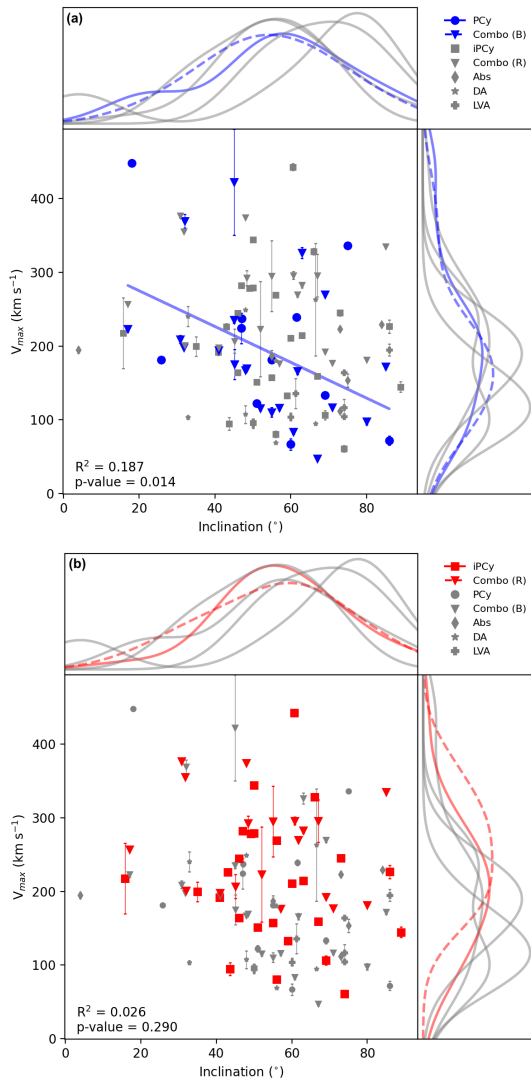


Fig. 9: Source inclinations with respect to the maximum velocities of observed absorption features (a) for the blue absorption features in P Cygni and combination profiles, and (b) for the red absorption features in inverse P Cygni and combination profiles in our sample. All other profile types are displayed in grey. The curves along the top and right-hand side are the kernel density estimation (KDE) of each profile type.

features for trends related to the source inclination and accretion properties. Finally, we examine the evolutionary trends observed in the data.

### 5.1. Pure emission

We observe 12 sources in Lupus without sub-continuum absorption features. Emission in the He I  $\lambda 10830$  Å line arises due to scattering and in situ emission. Pure emission profiles may arise due to a stellar wind, launched from high latitudes on the star and observed at typical inclinations of  $\approx 70^\circ$  (Kwan et al. 2007). Of the 12 stars with emission-only profiles, six targets have known jets. These are: Par-Lup3-4 (Whelan et al. 2014); Sz102 (Murphy et al. 2021); Sz69, Sz73, Sz123A and Sz123B which show both a high-velocity component (HVC) and low velocity component (LVC) in the [OI] $\lambda 6300$  Å line (Nisini et al. 2018). The HVC is generally attributed to high-velocity jets which can pro-

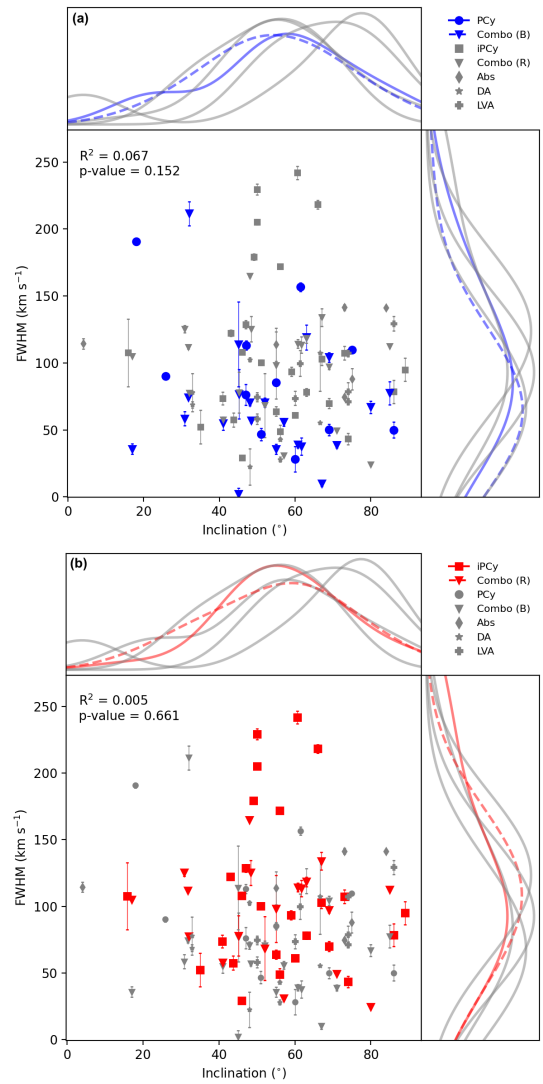


Fig. 10: Source inclinations with respect to the full-width half maximum of observed absorption features (a) for the blue absorption features in P Cygni and combination profiles, and (b) for the red absorption features in inverse P Cygni and combination profiles in our sample. All other profile types are displayed in grey. The curves along the top and right-hand side are the kernel density estimation (KDE) of each profile type.

duce either emission-only profiles (for edge-on sources) or P Cygni profiles (closer to pole-on) - see Section 5.2. A further four sources show signatures of a LVC, possibly a disk wind - these sources are Sz88A, Sz106, Sz133 and RX1556.1-3655 (Nisini et al. 2018).

Five sources (Par-Lup3-4, Sz102, Sz106, Sz123B, Sz133) are sub-luminous (sl) sources, which have a stellar luminosity much lower (by at least a factor ten) than other sources of the same spectral type (Alcalá et al. 2014; Nisini et al. 2018). Only three of the sub-luminous sources (Sz102, Sz123B and Sz133) have known inclinations, all of which are greater than  $40^\circ$ . Sub-luminous sources are generally expected to be observed edge-on (Hughes et al. 1994) but it is possible that the disk inclinations reported for these sources are underestimated, or that there is a misalignment between the inner and outer disk in some of these sources (Bohn et al. 2022) as previously mentioned. Jet morphology and proper motions of the Sz102 jet, for example, indi-



cate that the jet is in the plane of the sky (Murphy et al. 2021), i.e. the disk should be edge-on, thus revealing a possible misalignment between the inner and outer disk. Additionally, there are two other sub-luminous sources in the Lupus sample - these are Lup706 (an inverse P Cygni profile) and SSTc2dJ160703.9-391112 (absorption-only profile), so the lower luminosity is not unique to sources showing the emission-only profiles. Three of the sources with pure emission profiles exist in binary systems - these are Sz88A, and Sz123A and Sz123B (Alcalá et al. 2014). The inclination of the remaining source (J16085953-385627) with a pure emission profile is not known and it doesn't appear to be associated with any known jet.

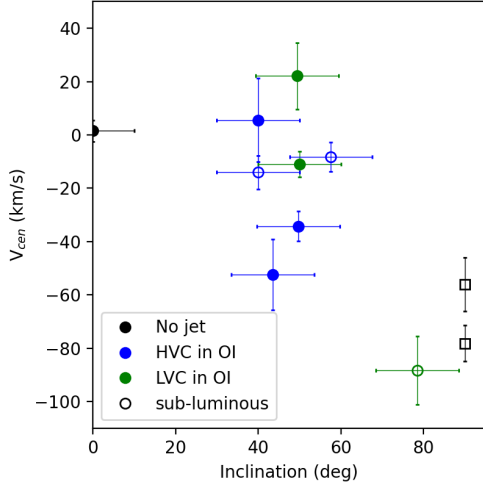


Fig. 11: Centroid velocities of the emission-only profiles versus the source inclination. Sub-luminous sources are plotted with the hollow markers. Square markers indicate sub-luminous sources with unknown inclinations.

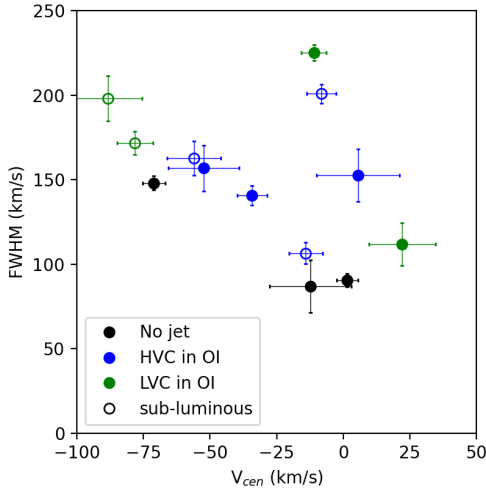


Fig. 12: FWHM versus the centroid velocity of the emission-only profiles. Sub-luminous sources are plotted with hollow markers.

We searched for a correlation between the centroid velocity of the emission profiles and the source inclination (see Figure 11). Generally, the centroid velocities were blue-shifted by up to  $100 \text{ km s}^{-1}$ , and those at higher velocities are narrower than the emission profiles closer to  $0 \text{ km s}^{-1}$  (see Figure 12). The fact that we tend to observe emission-only profiles for sources with

known jets and at high inclinations lends support to the models of Kwan et al. (2007). They note that when viewing the He I  $\lambda 10830 \text{ \AA}$  line for sources at higher inclinations, a stellar wind, which appears as a P Cygni profile for lower inclinations, may become an emission-only profile as the blue-shifted absorption feature becomes weaker and eventually disappears (see Figure 4). However, we note that for the 70 remaining sources in Lupus, 48 of the sources (68%) have a LVC and/or HVC signature in [OI] (Nisini et al. 2018). HVC signatures in [OI] are observed in sources with P Cygni profiles in the He I  $\lambda 10830 \text{ \AA}$  line at similar rates as the emission-only profiles - seven out of 11 P Cygni profiles in Lupus were observed with a HVC in [OI], compared to six of 12 emission-only profiles. Only ten sources with other profile types, however, are observed with a HVC in [OI]. Of the sources plotted in Figure 11, only one is not observed with either a LVC or HVC in OI - this source is Lup607 which has an inclination of  $0^\circ$ . The inclinations of the other two sources without a known jet or outflow (J16085953-3856275 and SSTc2dJ160708.6-391408) are not known. Further, in Figure 11, we plot the sub-luminous sources without known inclinations at  $90^\circ$  (in line with the assumption that sub-luminous sources are often viewed edge-on). These sources show centroid velocities that are blue-shifted to velocities up to  $-80 \text{ km s}^{-1}$ , in line with the apparent correlation of centroid velocity and source inclination for the emission profiles. However, if the inclinations for the two sub-luminous sources located at  $\sim 40\text{--}60^\circ$  are underestimated, the correlation between centroid velocity and inclination is less evident if these sources are closer to edge-on ( $> 70^\circ$ ). It is also possible that disk occultation may result in the emission profile becoming blue-shifted, which could explain a trend in the centroid velocity with respect to source inclination.

In a number of emission-only sources (e.g. Sz73, Sz88A, Sz102 and SSTc2dJ160708.6-391408), we observe asymmetric line profiles as is often seen in forbidden emission lines (for example, by Nisini et al. 2018; Banzatti et al. 2019). While the majority of our targets with emission-only profiles are associated with known jets, these profiles can still be produced in other scenarios. For example, in Figures C.1 and C.2, where we show all Lupus profiles arranged by profile type, we see a number of asymmetric emission profiles (e.g. Par-Lup3-4, Sz73, Sz106, Sz133 and RX1556.1-3655), which appear to have low-velocity absorption features that are not sub-continuum, and thus not fitted by our fitting routine. This is also the case in the Taurus sample studied by Edwards et al. (2006), where four targets show asymmetric emission profiles indicating possible red and/or blue absorption that is not sub-continuum. Overall, we find that sources showing an emission-only profile tend to be associated with known jets and outflows, and appear at high source inclinations.

## 5.2. Profiles with absorption features

We observe absorption features in many spectra from both regions in our sample. In the following sections we discuss observed trends in velocities of the wind and accretion features, and investigate if the measured absorption velocities have any dependence on the source inclination and/or accretion properties.

### 5.2.1. Velocity of the absorption features

**Absorption features tracing winds** In Figure 8, we present histograms of the difference between our observed blue-shifted

velocities and the escape velocities from the star. Eleven sources show  $v_{\max}$  lower than the escape velocity (i.e. below  $0 \text{ km s}^{-1}$  in Figure 8), of which seven sources have known inclinations. These sources occur across the range of source inclinations, so this is not thought to be an effect of the viewing angle. Thus where the measured velocities are lower than the escape velocity, we suggest that not only gravitational forces act on the wind, but that there may also be magnetic fields at play. In wind launching models, it is assumed that the wind can be accelerated to a few times the escape velocity at the launching radius, especially in MHD launching models (see review by Pudritz et al. 2007). However, if we are tracing disk winds, the escape velocity from the disk would be much lower than the stellar escape velocity. It is possible to distinguish between which type of wind based on the widths of the blue absorption features in the He I  $\lambda 10830 \text{ \AA}$  profiles. Narrower blue absorptions at low velocities are generally attributed to disk winds, while wider features across a range of velocities are more likely to originate in stellar winds (Edwards et al. 2006; Kwan et al. 2007).

**Absorption features tracing accretion** In Figure 8, we also plot the difference between our observed red-shifted velocities and the free-fall velocities. In the top panel, a number of sources have observed red-shifted velocities less than free-fall velocities. Hartmann et al. (2016) note that magnetospheric accretion models assume free-fall along axisymmetric, dipolar magnetic field lines at a constant infall rate. For measured  $v_{\max}$  lower than the expected free-fall velocities, it is possible that the material has simply not yet reached its terminal speed. Cauley & Johns-Krull (2014, 2015) suggest that the maximum velocities can be lower than free-fall velocities in cases where the magnetospheric accretion geometry is more compact due to a weaker magnetic field. On the other hand, for larger values of  $v_{\max}$ , the general assumptions of axisymmetric and dipolar magnetic fields may not apply and more complex fields may be present. For example, Gregory et al. (2012) have derived magnetic field maps for a number of T Tauri stars and find that the large-scale magnetic field topology can vary substantially with stellar properties, often finding non-axisymmetric fields with strong multipolar components. Further, typical  $3\sigma$  errors on the measured velocities are, on average, a few tens of  $\text{km s}^{-1}$ , which cannot explain why some sources have  $v_{\max}$  approximately  $100 \text{ km s}^{-1}$  greater than the free-fall velocity.

Thus, the velocities of the absorption features in the He I  $\lambda 10830 \text{ \AA}$  line profiles may reveal information about the geometry of both the outflow(s) and the accretion flows in the system.

### 5.2.2. Dependence on source inclination

The inclination of the source can affect the observed profiles, thus in Figures 9 & 10 we compare the maximum velocity and the widths of the absorption features to the inclination. In these figures, the curves along the top and right-hand side are the kernel density estimation (KDE) of each profile type which we use to estimate, for example, the most likely inclination at which a certain profile type is observed. The blue points in panel (a) represent the P Cygni profiles and blue feature in combination profiles, while the red points (panel (b)) represent the inverse P Cygni profiles and the red feature in combination profiles. Only the blue or red points are fitted with a line of best fit. The grey points in these panels represent all the other profile types, and are plotted only for comparison with the highlighted blue or red data points. We use the  $R^2$  values and p-values as a measure of the goodness of each fit. The  $R^2$  value is a measure of the scatter

in our data, while the p-value measures the likelihood that any observed trends are significant and not a result of chance. A high  $R^2$  indicates a small scatter and a good linear fit, but we tend to observe low  $R^2$  values due to large scatter. Instead, the p-value gives us a better indication as to whether or not there is a significant trend between, for example, the maximum velocity and the inclination. Generally, a p-value lower than 0.05 is accepted as evidence of a relationship between two variables.

**Absorption features tracing winds** With the exception of a few sources, blue-shifted absorption features are generally not observed at low inclinations ( $< 40^\circ$ ). However, we do see a slight trend in the blue-shifted velocities, as the lowest velocities are present at high inclinations, suggesting that we observe different velocity components of the wind at different relative inclinations to the star. This dependence on inclination is also seen in models of the He I  $\lambda 10830 \text{ \AA}$  line (e.g. Kwan et al. 2007), and is likely due to changing line-of-sight velocities when viewing the wind at different inclinations (Kurosawa & Romanova 2012). This is illustrated by Xu et al. (2021) and in Figure 4, where at higher inclinations (edge-on) absorption features are created by lower velocity disk winds leading to less blue-shifted and narrow features. The blue-shifted features appear narrower than their red-shifted counterparts, which was generally seen in previous observations of a smaller sample (Edwards et al. 2006). In Figure 10 panel (a), a number of blue-shifted absorption features have FWHMs of  $\sim 50 \text{ km s}^{-1}$ , particularly for combination profiles. We note however that the blue-shifted features become slightly narrower at high inclinations, thus knowledge of the viewing angle is important to determine which type of wind is present. Our measured velocities and widths of the blue-shifted absorption features are consistent with previous studies, for example Kwan et al. (2007), that find that the blue-shifted features in P Cygni profiles are expected to become less blue-shifted and narrower as the inclination changes from face-on (0 degrees) to edge-on (90 degrees).

**Absorption features tracing accretion** Red-shifted velocities appear to be more independent of the source inclination. We see a majority of red-shifted velocities near  $\approx 200 - 250 \text{ km s}^{-1}$  tailing off to higher velocities up to  $\approx 400 \text{ km s}^{-1}$ , but with no significant decrease in velocity at higher inclinations. Further, these velocities are consistent with free-fall velocities for stellar radii between  $R_\star = 1 - 2 R_\odot$  assuming a magnetospheric radius of  $R_M = 5 R_\star$  (Hartmann et al. 2016) (see Figure 6). This is similar to the calculations of Kwan & Fischer (2011) who found that infalling gas can reach speeds of  $150 \text{ km s}^{-1}$  near  $2 R_\star$  if the accretion flow starts between  $4 - 8 R_\star$ . Previous models of the red-shifted absorption in the He I  $\lambda 10830 \text{ \AA}$  line for a star with a dipolar magnetic field showed narrowing of the absorption at higher inclinations (Fischer et al. 2008), suggesting that the sources in our sample may have a more complex magnetic field than the dipolar axisymmetric fields normally assumed in models of magnetospheric accretion (Hartmann et al. 2016). We do not observe such a trend in the measured velocities and widths of the red-shifted absorption features in our sample. We also reiterate that the inclinations presented in these plots are for the outer disk, which may be misaligned from the inner disk (Bohn et al. 2022).

### 5.2.3. Dependence on accretion properties

In Figure 13, for each profile type we plot the ratio of the accretion luminosity to the stellar luminosity with respect to the stellar luminosity. P Cygni profiles are observed over a range of accretion luminosities, while inverse P Cygni and combination profiles have stronger peaks in their distribution across the range of accretion luminosities. The ratio of  $L_{\text{acc}}/L_{\star}$  varies for each of these profile types, with a bimodal distribution in the P Cygni profiles (peaking at  $\log(L_{\text{acc}}/L_{\star}) \approx -1.0$  and a second peak at  $\approx -3.0$ ), however low number statistics brings into question the significance of the bi-modality. Single peaks are observed for the inverse P Cygni profiles (at  $\log(L_{\text{acc}}/L_{\star}) \approx -2.0$ ) and combination profiles (at  $\log(L_{\text{acc}}/L_{\star}) \approx -1.2$ ). These results appear to show that profiles with blue-shifted absorption features, tracing the presence of an outflow, occur in sources with higher accretion rates. Recent models of disk evolution have shown that MHD disk winds in particular can account for the observed accretion properties of young stars in Lupus (Tabone et al. 2021), suggesting that accretion is an important part of driving winds and outflows. If these winds are indeed accretion-powered, as suggested by Edwards et al. (2006), this result shows that the He I  $\lambda 10830$  Å line is a useful way to probe the connection between accretion and ejection.

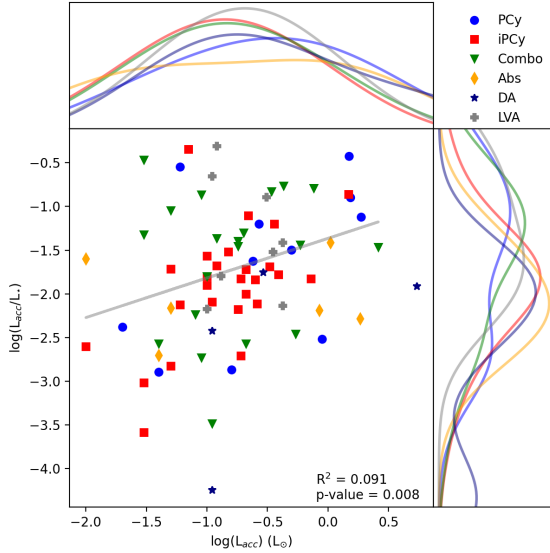


Fig. 13:  $L_{\text{acc}}/L_{\star}$  versus the accretion luminosity  $L_{\text{acc}}$  for all profile types with absorption features.

We find that targets with blue absorption features (i.e. P Cygni or combination profiles) have slightly stronger accretion than those targets with only red absorption (i.e. inverse P Cygni profiles). This however seems to be driven mostly by the number of combination profiles present at higher accretion luminosities. Nonetheless, the higher accretion rates observed for targets with blue absorption features supports the findings of Edwards et al. (2006), who observe stellar winds at targets with a wide range of accretion rates.

In Figure 14 we plot the Gaussian area (in units of  $\text{km s}^{-1} \times \text{normalised flux units}$ ) of the absorption features in our spectra, which is proportional to the column density of the in-falling/outflowing gas, and thus can be related to the mass accretion or mass ejection rates. In general, we find that sources with higher accretion luminosities tend to have larger absorption features in the He I  $\lambda 10830$  Å line profile. Given that the red-shifted

absorption features trace accretion, we would expect these profiles (i.e. inverse P Cygni and combination) to have higher accretion luminosities than profiles with only blue absorption features. Instead, from the curves along the top of each panel in Figure 14, we see that P Cygni profiles peak at higher accretion luminosities ( $\log(L_{\text{acc}}) \approx -2$   $L_{\odot}$ ) than inverse P Cygni and combination profiles (which peak at  $\log(L_{\text{acc}}) \approx -3$   $L_{\odot}$ ).

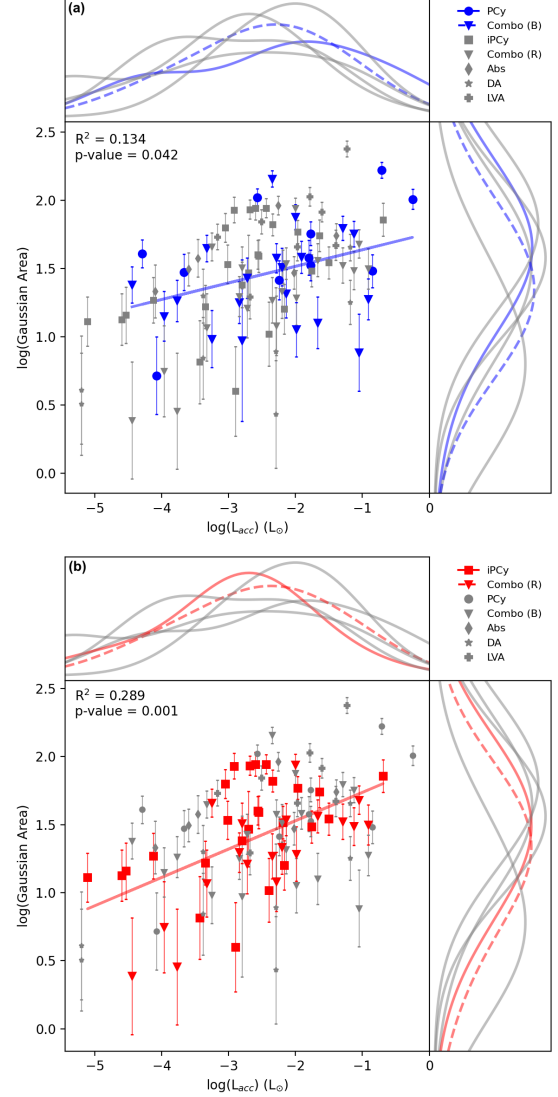


Fig. 14: Gaussian area, in units of  $\text{km s}^{-1} \times \text{normalised flux units}$ , of the observed absorption features in our spectra, with respect to the accretion luminosity, for the (a) P Cygni and blue combination profile absorption features, and (b) inverse P Cygni and red combination profile absorption features.

We investigate the combination profiles in more depth in Figure 15, where we present the ratio of the Gaussian area of the blue-shifted absorption feature divided by that of the red-shifted feature. In this plot there is a trend towards higher accretion luminosities where this ratio is close to or equal to one (dashed line), i.e. when the blue- and red-absorption features are most similar. We note however that the p-value of the linear fits for both the blue and red points was 0.15, i.e. the trend is not statistically significant. This is thought to be due to small number statistics (18 sources in Figure 15).

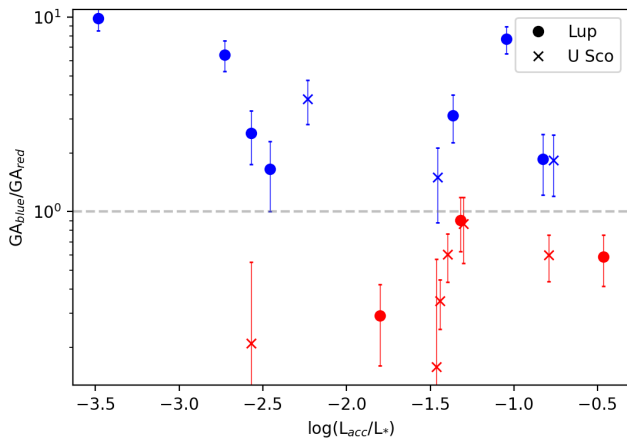


Fig. 15: Plot of the Gaussian area, in units of  $\text{km s}^{-1} \times \text{normalised flux units}$ , of the blue-shifted absorption feature divided by that of the red-shifted feature for combination profiles. Combination profiles in Lupus are denoted by circle markers, and those in Upper Sco are marked by an X. The horizontal dashed line (where the ratio is equal to 1) marks where the area of the blue and red features are equal. Blue or red coloured markers indicate blue- or red-dominated sources.

### 5.3. Evolutionary trends

In Figure 5, the proportion of each profile type in both star-forming regions of our sample is presented in comparison to that of the Taurus sample of Edwards et al. (2006). Given that the ages of Taurus and Lupus are similar ( $< 3$  Myr Luhman et al. 2010; Comerón 2008), we would expect the proportions of each profile type in these two regions to be similar. However, we note large differences in the proportions of the three most common profile types (P Cygni, inverse P Cygni, and combination profiles) between the Taurus and Lupus regions. As noted previously, this is not thought to be due to instrumental effects. It is also important to note that the classification of profile types in the He I  $\lambda 10830$  Å line varies through the literature. For example, Edwards et al. (2006) define only five distinct profile types, while Thanathibodee et al. (2022) identifies six profile types, compared to the eight types we observe. It could be that the double absorption profiles observed in our sample, for example, are in fact combination profiles with no emission feature. In this case, the number of combination profiles in Lupus becomes 16 ( $\approx 20\%$ ) compared to 15 ( $\approx 39\%$ ) in Taurus. This still does not explain the large difference in the number of P Cygni and inverse P Cygni profiles in each region. However, we note that certain regions of the Lupus and Taurus clouds have varying ages and this may suggest that younger sources with outflow phenomena are more common in Taurus.

Between the Lupus and Upper Sco regions from our sample, we find two notable differences in the proportions of each of the three most common profile types (P Cygni, inverse P Cygni, and combination profiles). Firstly, the emission-only profiles disappear entirely in our Upper Sco sample. In Section 5.1 we suggest that the emission-only profiles are the result of jets or winds. If this is indeed the case, this suggests that the jet disappears early on, before the age of the Upper Sco sources. In Figure 16, we present the Gaussian area, in units of  $\text{km s}^{-1} \times \text{normalised flux units}$ , of the emission features in all emission-only, P Cygni, inverse P Cygni, and combination profiles in both regions. We compare the Gaussian area of the emission features to the ratio

of the accretion luminosity to the stellar luminosity for Lupus (black circles) and Upper Sco (green squares). In general, the size of the emission features in Upper Sco is smaller than in Lupus, and only becomes comparable at high  $L_{\text{acc}}/L_{\star}$ . In both regions there is a strong trend of the emission with  $L_{\text{acc}}/L_{\star}$  suggesting that at least some of the emission originates from the accretion shocks on the stellar surface. Further, this trend supports the results of Kwan et al. (2007), who suggest that stars with higher accretion rates are more likely to exhibit stellar wind signatures.

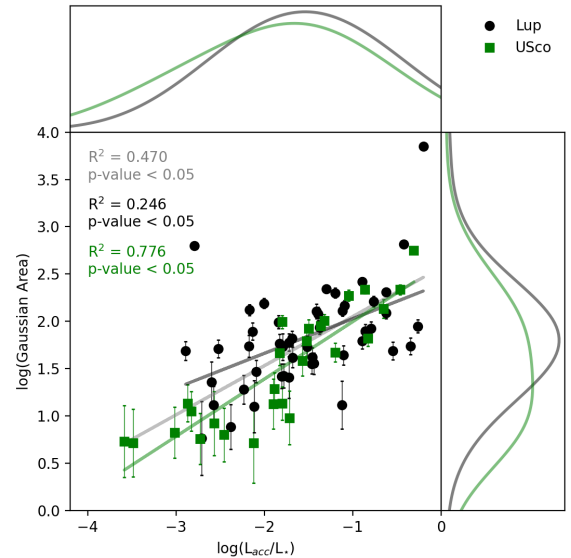


Fig. 16: Gaussian area, in units of  $\text{km s}^{-1} \times \text{normalised flux units}$ , versus  $\log(L_{\text{acc}}/L_{\star})$  of the emission features in pure emission, P Cygni, inverse P Cygni and combination profile types separated by star-forming region. The line of best fit for all datapoints is marked in grey, with a linear fit for Lupus and Upper Sco in black and green, respectively.

The second difference between the Lupus and Upper Sco regions in Figure 5 is the significant increase in the proportion of combination profiles, up to  $\approx 30\%$  in Upper Sco. This suggests that the sources in Upper Sco are still actively accreting, while the blue-shifted features in the combination profiles means that winds and outflows are also present. In Figure 15, we also distinguish the ratio of the Gaussian areas of the absorption features in combination profiles between both regions. We find that the majority of the Lupus combination profiles (seven of 10) have a larger blue-shifted feature, while combination profiles in Upper Sco (seven of 9) tend to be dominated by the red-shifted feature, indicating that the winds detected in the Lupus sample are stronger than those in Upper Sco. This also indicates a difference in the accretion in both regions. However, Manara et al. (2020) found similar values for the mass accretion rates in Lupus and Upper Sco, so this is not likely to be the reason for the increased proportion of combination profiles. We note that the absolute number of combination profiles in Lupus and Upper Sco is similar (12 and 11, respectively) so we cannot rule out the possibility that this difference between the two regions is due to the small sample size.

## 6. Conclusions

In this work, we present X-Shooter observations of the He I  $\lambda 10830$  Å line from a sample of 107 young stellar objects in

the Lupus and Upper Scorpius star forming regions. We characterised the line profiles into one of eight profile types to search for any significant trends in our data with age, source inclination and accretion properties. Our main conclusions are as follows:

- We observe variations in the proportions of each profile type between the two star forming regions, particularly in the number of profiles with both blue- and red-shifted absorption features. In Lupus, a large proportion of the targets (33%) have inverse P Cygni profiles, followed by roughly equal proportions of P Cygni (13%) and combination profiles (15%). Meanwhile, in Upper Scorpius, the most common profile types are the combination and inverse P Cygni profile types ( $\approx 33\%$  each), with fewer P Cygni profiles (28%) observed. In contrast, Edwards et al. (2006) observed a larger number of P Cygni profiles and fewer inverse P Cygni profiles in the Taurus sample.
- The observed maximum velocities of the absorption features are consistent with the expected free-fall, but are larger than the escape velocities of our targets. The free-fall velocities are consistent with the observed velocities in the majority of targets. However, some sources show observed maximum velocities which differ from the expected free-fall velocity which may occur if we are observing material which has not reached the terminal velocity yet, or may be related to the accretion geometry and magnetic field. Generally, the outflowing gas (traced by the blue absorption features), has a velocity larger than the escape velocity, however, magnetic fields associated with MHD disk winds may explain the launching of this material from sources with velocities smaller than the escape velocity.
- We find a correlation between the maximum velocities and the source inclination, and this correlation is stronger for sources with blue absorption features than those with only red features. This implies that different velocity components of the wind are observed at different inclinations, as suggested by models of the He I  $\lambda 10830$  Å line (Kwan et al. 2007).
- The full-width half-maximum of the absorption features show less of a correlation with the source inclination than the velocities, which is important to note if we aim to discriminate between a stellar wind or disk wind. Further, our results are consistent with previous works by Edwards et al. (2006); Kwan et al. (2007); Fischer et al. (2008) where the maximum absorption velocities also appeared to be dependent on the viewing angle.
- We typically observe different accretion rates for each profile type in our sample. We see higher accretion rates in targets where the He I  $\lambda 10830$  Å line profile has a blue-shifted absorption feature, supporting the idea that these winds are in fact accretion-powered (Edwards et al. 2006). This argument is again strengthened when examining the combination profiles, which show the highest accretion rates when the blue and red-shifted absorption features are similar in size.
- The observed differences in the proportion of emission-only profiles may suggest that jets or winds are more common in younger sources, and may disappear entirely quite early on (ages  $< 5$  Myr). Meanwhile, the increase in the proportion of combination profiles is not linked to differences in accretion between both regions, and may be due to the smaller sample in Upper Sco.

In our study of over 100 sources in Lupus and Upper Sco, we build on previous works by providing statistics for a larger sample of stars than before. We find that the He I  $\lambda 10830$  Å line

is a particularly good tracer of both infalling and outflowing gas in the inner disk. Future studies of even larger samples, and in star-forming regions of different ages, could reveal evolutionary trends in accretion and ejection signatures in young stars. Future work would also benefit from a clearer understanding of inner disk inclinations and any misalignment with the outer disk. Enlarging the statistics on He I  $\lambda 10830$  Å line properties will allow us to confirm our results and past results, and further our understanding of the accretion-ejection connection in the innermost regions of protoplanetary disks.

**Acknowledgements.** We thank the ESO staff in Paranal for carrying out the observations in Service mode. We thank S. Edwards and A. Natta for insightful discussions and feedback on this work, and G. Beccari for the support during this work. This work benefited from discussions with the ODYSSEUS team (HST AR-16129), <https://sites.bu.edu/odysseus/>. JE acknowledges the ESO Studentship program funded by the Irish Research Council and Teaching Assistantship funding from the School of Physics, University College Dublin. Funded by the European Union under the European Union's Horizon Europe Research & Innovation Programme 101039452 (WANDA). Views and opinions expressed are however those of the author(s) only and do not necessarily reflect those of the European Union or the European Research Council. Neither the European Union nor the granting authority can be held responsible for them. This research received financial support from the project PRIN-INAF 2019 "Spectroscopically Tracing the Disk Dispersal Evolution". MV acknowledges support from ESA through the Leiden/ESA Astrophysics Program for Summer Students (LEAPS) 2015. We made use of PyAstronomy and Astropy for this work.

## References

- Alcalá, J. M., Manara, C. F., France, K., et al. 2019, *A&A*, 629, A108  
 Alcalá, J. M., Manara, C. F., Natta, A., et al. 2017, *A&A*, 600, A20  
 Alcalá, J. M., Natta, A., Manara, C. F., et al. 2014, *A&A*, 561, A2  
 Ansdell, M., Williams, J. P., Trapman, L., et al. 2018, *ApJ*, 859, 21  
 Arce, H. G., Shepherd, D., Gueth, F., et al. 2007, in *Protostars and Planets V*, ed. B. Reipurth, D. Jewitt, & K. Keil, 245  
 Bai, X.-N. 2016, *ApJ*, 821, 80  
 Banzatti, A., Pascucci, I., Edwards, S., et al. 2019, *ApJ*, 870, 76  
 Barenfeld, S. A., Carpenter, J. M., Ricci, L., & Isella, A. 2016, *ApJ*, 827, 142  
 Barenfeld, S. A., Carpenter, J. M., Sargent, A. I., Isella, A., & Ricci, L. 2017, *ApJ*, 851, 85  
 Beristain, G., Edwards, S., & Kwan, J. 2001, *ApJ*, 551, 1037  
 Blandford, R. D. & Payne, D. G. 1982, *MNRAS*, 199, 883  
 Bohn, A. J., Benisty, M., Perraut, K., et al. 2022, *A&A*, 658, A183  
 Cabrit, S., Edwards, S., Strom, S. E., & Strom, K. M. 1990, *ApJ*, 354, 687  
 Carpenter, J. M., Mamajek, E. E., Hillenbrand, L. A., & Meyer, M. R. 2006, *ApJL*, 651, L49  
 Cauley, P. W. & Johns-Krull, C. M. 2014, *ApJ*, 797, 112  
 Cauley, P. W. & Johns-Krull, C. M. 2015, *ApJ*, 810, 5  
 Comerón, F. 2008, *The Lupus Clouds*, Vol. 5 (Sky ASP Monograph Publications), 295  
 Edwards, S. 2009, in *American Institute of Physics Conference Series*, Vol. 1094, 15th Cambridge Workshop on Cool Stars, Stellar Systems, and the Sun, ed. E. Stempels, 29–38  
 Edwards, S., Fischer, W., Hillenbrand, L., & Kwan, J. 2006, *ApJ*, 646, 319  
 Edwards, S., Fischer, W., Kwan, J., Hillenbrand, L., & Dupree, A. K. 2003, *ApJ*, 599, L41  
 Ercolano, B. & Pascucci, I. 2017, *Royal Society Open Science*, 4, 170114  
 Ferreira, J., Dougados, C., & Cabrit, S. 2006, *A&A*, 453, 785  
 Fischer, W., Edwards, S., Hillenbrand, L., & Kwan, J. 2011, *ApJ*, 730, 73  
 Fischer, W., Kwan, J., Edwards, S., & Hillenbrand, L. 2008, *ApJ*, 687, 1117  
 Folha, D. F. M. & Emerson, J. P. 1999, *A&A*, 352, 517  
 Frank, A., Ray, T. P., Cabrit, S., et al. 2014, *Protostars and Planets VI*, 451  
 Frasca, A., Biazzo, K., Alcalá, J. M., et al. 2017, *A&A*, 602, A33  
 Gaia Collaboration. 2018, *A&A*, 616, A1  
 Gregory, S. G., Donati, J. F., Morin, J., et al. 2012, *ApJ*, 755, 97  
 Hartigan, P., Edwards, S., & Ghandour, L. 1995, *ApJ*, 452, 736  
 Hartmann, L., Calvet, N., Gullbring, E., & D'Alessio, P. 1998, *ApJ*, 495, 385  
 Hartmann, L., Herczeg, G., & Calvet, N. 2016, *ARA&A*, 54, 135  
 Hughes, J., Hartigan, P., Krautter, J., & Kelemen, J. 1994, *AJ*, 108, 1071  
 Kausch, W., Noll, S., Smette, A., et al. 2015, *A&A*, 576, A78  
 Krolkowski, D. M., Kraus, A. L., & Rizzuto, A. C. 2021, *AJ*, 162, 110  
 Kurosawa, R. & Romanova, M. M. 2012, *MNRAS*, 426, 2901  
 Kwan, J., Edwards, S., & Fischer, W. 2007, *ApJ*, 657, 897  
 Kwan, J. & Fischer, W. 2011, *MNRAS*, 411, 2383  
 Luhman, K. L. 2020, *AJ*, 160, 186



- Luhman, K. L. 2022, *AJ*, 163, 24
- Luhman, K. L., Allen, P. R., Espaillat, C., Hartmann, L., & Calvet, N. 2010, *ApJS*, 186, 111
- Luhman, K. L. & Mamajek, E. E. 2012, *ApJ*, 758, 31
- Manara, C. F., Ansdell, M., Rosotti, G. P., et al. 2022, *arXiv e-prints*, [arXiv:2203.09930](#)
- Manara, C. F., Morbidelli, A., & Guillot, T. 2018, *A&A*, 618, L3
- Manara, C. F., Natta, A., Rosotti, G. P., et al. 2020, *A&A*, 639, A58
- McJunkin, M., France, K., Schneider, P. C., et al. 2014, *ApJ*, 780, 150
- Modigliani, A., Goldoni, P., Royer, F., et al. 2010, in *Society of Photo-Optical Instrumentation Engineers (SPIE) Conference Series*, Vol. 7737, *Observatory Operations: Strategies, Processes, and Systems III*, ed. D. R. Silva, A. B. Peck, & B. T. Soifer, 773728
- Murphy, A., Dougados, C., Whelan, E. T., et al. 2021, *A&A*, 652, A119
- Natta, A., Testi, L., Alcalá, J. M., et al. 2014, *A&A*, 569, A5
- Nisini, B., Antonucci, S., Alcalá, J. M., et al. 2018, *A&A*, 609, A87
- Pascucci, I., Cabrit, S., Edwards, S., et al. 2022, *arXiv e-prints*, [arXiv:2203.10068](#)
- Pecaut, M. J., Mamajek, E. E., & Bubar, E. J. 2012, *ApJ*, 746, 154
- Pudritz, R. E. & Norman, C. A. 1983, *ApJ*, 274, 677
- Pudritz, R. E., Ouyed, R., Fendt, C., & Brandenburg, A. 2007, in *Protostars and Planets V*, ed. B. Reipurth, D. Jewitt, & K. Keil, 277
- Pudritz, R. E. & Ray, T. P. 2019, *Frontiers in Astronomy and Space Sciences*, 6, 54
- Shu, F., Najita, J., Ostriker, E., et al. 1994, *ApJ*, 429, 781
- Smette, A., Sana, H., Noll, S., et al. 2015, *A&A*, 576, A77
- Tabone, B., Rosotti, G. P., Lodato, G., et al. 2021, *MNRAS Letters*, 512, L74
- Tazzari, M., Testi, L., Natta, A., et al. 2017, *A&A*, 606, A88
- Thanathibodee, T., Calvet, N., Hernández, J., Maucó, K., & Briceño, C. 2022, *AJ*, 163, 74
- Vernet, J., Dekker, H., D’Odorico, S., et al. 2011, *A&A*, 536, A105
- Virtanen, P., Gommers, R., Oliphant, T. E., et al. 2020, *Nature Methods*, 17, 261
- Vorobyov, E. I., Elbakyan, V. G., Plunkett, A. L., et al. 2018, *A&A*, 613, A18
- Whelan, E. T., Bonito, R., Antonucci, S., et al. 2014, *A&A*, 565, A80
- Xu, Z., Herczeg, G. J., Johns-Krull, C. M., & France, K. 2021, *ApJ*, 921, 181
- Yen, H.-W., Koch, P. M., Manara, C. F., Miotello, A., & Testi, L. 2018, *A&A*, 616, A100
- Zhang, Y., Arce, H. G., Mardones, D., et al. 2019, *ApJ*, 883, 1

Table 1: Observed profile types, emission centroid velocity and absorption centroid velocities in the Lupus sample. Stellar radii and the calculated escape and free-fall velocities are also listed.

Object	Fit	Profile Type	$V_{em}$ (km s <sup>-1</sup> )	$V_{abs}$ (km s <sup>-1</sup> )	$R_{\star}$ ( $R_{\odot}$ )	$V_{esc}$ (km s <sup>-1</sup> )	$V_{ff}$ (km s <sup>-1</sup> )
Sz66		iPCy	-53.88	17.53	1.34	287.09	260.29
AKC2006-19		PCy	26.97	-31.05	0.48	332.42	301.40
Sz69		Em	-52.28		0.98	279.08	253.03
Sz71		iPCy	-49.65	98.22	1.45	328.05	297.43
Sz72	M	PCy	-65.47	-196.31	1.37	321.18	291.20
Sz73	M	Em	-34.23		1.37	532.32	482.63
Sz74	M	PCy	24.32	-65.33	3.22	188.58	170.98
Sz83	M	PCy	-10.53	-204.98	2.47	346.99	314.60
Sz84	M	iPCy	-48.76	16.41	1.23	236.07	214.03
Sz130		Combo	2.98	-64.98	1.12	417.30	378.35
				170.18			
Sz88A	M	Em	-10.95		1.58	476.99	432.47
Sz88B	M	Combo	27.41	-12.55	1.82	204.86	185.74
				175.06			
Sz91	M	Combo	-30.0	-77.2	1.09	423.01	383.53
				164.26			
Lup713		iPCy	-34.62	103.91	0.51	288.25	261.35
Lup604s		DA		-9.26	0.71	253.17	229.54
				113.76			
Sz97	M	iPCy	-102.39	81.98	1.04	297.40	269.64
Sz99	M	iPCy	0.0	83.52	0.70	354.57	321.48
Sz100		Combo	-12.52	-77.39	1.01	212.89	193.02
				107.47			
Sz103	M	iPCy	-114.38	-17.67	1.08	284.87	258.28
Sz104		Combo	-2.58	-59.24	0.90	259.82	235.57
				108.29			
Lup706	M	iPCy	-63.64	50.0			
Sz106		Em	-78.15		0.57	616.00	558.50
Par-Lup3-3		iPCy	19.66	136.19	1.21	269.42	244.27
Par-Lup3-4		Em	-56.02				
Sz110		Combo	-13.97	-174.80	1.32	257.41	233.39
				132.01			
Sz111		iPCy	-109.70	76.29	1.11	417.88	378.88
Sz112	M	Combo	-9.89	-60.22	1.18	234.05	212.21
				91.01			
Sz113	M	PCy	-10.78	-147.44			
2MASSJ16085953-3856275		Em	-12.30		0.49	152.25	138.04
SSTc2d160901.4-392512	M	iPCy	-62.88	-10.34	0.99	298.16	270.33
Sz114	M	iPCy	22.42	80.51	1.52	218.57	198.17
Sz115		Abs		-15.58	1.08	265.43	240.65
Lup818s		iPCy	-24.91	85.09	0.53	240.43	217.99
Sz123A	M	Em	5.59		0.88	543.99	493.22
Sz123B	M	Em	-14.05		0.46	578.41	524.42
SST-Lup3-1		PCy	72.55	108.47	1.71	189.00	171.36
Sz65		PCy	19.81	-439.49	1.91	373.91	339.01
AKC2006-18		iPCy	3.02	133.01	0.39	262.54	238.03
SSTc2dJ154508.9-341734		PCy	-40.24	-127.07	0.87	238.34	216.09
Sz68		DA		-141.33			
				15.77			
SSTc2dJ154518.5-342125		PCy	-15.97	-66.31	0.77	252.99	229.37
Sz81A		Abs		-100.49	1.03	291.78	264.54
Sz81B		DA		-125.68	1.67	185.01	167.74
				15.29			
Sz129		Combo	0.60	-103.65	1.33	533.35	483.57
				212.72			
SSTc2dJ155925.2-423507		Combo	6.07	-134.31	0.48	332.42	301.40
				143.03			
RY Lup		PCy	36.31	-72.47			
SSTc2dJ160000.6-422158		iPCy	-128.615	-38.28	0.65	358.82	325.33

SSTc2dJ160002.4-422216	M	Abs		86.80	1.32	257.41	233.39
SSTc2dJ160026.1-415356		iPCy	3.75	117.0	1.01	230.17	208.69
MY Lup		Abs		-43.01	1.18	565.02	512.29
Sz131	M	iPCy	-71.51	13.46	1.11	321.34	291.35
Sz133		Em	-88.30				
SSTc2dJ160703.9-391112		Abs		-11.43			
Sz90	M	LVA	-8.88	8.86	1.31	568.08	515.06
Sz95	M	Combo	-108.51	-13.03	1.46	346.79	314.42
				100.0			
Sz96	M	LVA	-24.56	2.72	1.58	330.08	299.27
2MASSJ16081497-3857145	M	Abs		41.41	0.36	327.16	296.62
Sz98	M	PCy	-46.63	-92.88	2.50	456.82	414.18
Lup607	M	Em	1.52		0.87	199.08	180.50
Sz102		Em	-8.23				
SSTc2dJ160830.7-382827		Abs		-16.80			
SSTc2dJ160836.2-392302	M	Misc	1.49	-180.90	2.02	511.84	464.07
				-12.24			
				100.0			
Sz108B	M	Combo	-80.37	10.97	1.13	239.20	216.87
				100.0			
2MASSJ16085324-3914401		Combo	41.55	-33.77	1.31	290.45	263.34
				150.35			
2MASSJ16085529-3848481		iPCy	16.60	115.96	0.87	199.08	180.50
SSTc2dJ160927.0-383628		iPCy	-71.56	23.62	0.86	318.99	289.21
Sz117		iPCy	-47.30	123.37	1.58	245.45	222.54
Sz118		iPCy	-89.95	28.03	1.50	514.88	466.82
2MASSJ16100133-3906449		iPCy	45.07	133.03			
SSTc2dJ161018.6-383613		Abs		22.73	0.68	289.34	262.34
SSTc2dJ161019.8-383607	M	Abs		42.15	0.77	221.88	201.17
SSTc2dJ161029.6-392215		DA		-24.37	1.08	265.68	240.88
				126.37			
SSTc2dJ161243.8-381503		iPCy	-70.65	21.68	1.52	336.25	304.87
SSTc2dJ161344.1-373646	M	PCy	1.52	-78.32	0.68	308.03	279.28
Sz75/GQ Lup	M	Combo	-85.14	0.0	2.30	364.57	330.54
				161.403			
Sz76		Misc	33.56	-108.97	1.32	278.90	252.87
				-20.24			
				132.09			
Sz77		Combo	-18.51	-117.90	1.56	428.92	388.89
				125.19			
RXJ1556.1-3655		Em	22.10		1.24	388.31	352.07
Sz82/IM Lup		Combo	-7.86	-97.27	2.84	356.98	323.66
				132.78			
EX Lup		Combo	0.736	-134.77	1.96	320.94	290.993
				217.083			

**Notes.** An 'M' in column 2 is spectra that was fit using manually defined initial guesses

Table 2: Observed profile types, emission centroid velocity and absorption centroid velocities in the Upper Scorpius sample. Stellar radii and the calculated escape and free-fall velocities are also listed.

Object	Fit	Profile Type	$V_{em}$ (km s <sup>-1</sup> )	$V_{abs}$ (km s <sup>-1</sup> )	$R_{\star}$ ( $R_{\odot}$ )	$V_{esc}$ (km s <sup>-1</sup> )	$V_{ff}$ (km s <sup>-1</sup> )
2MASSJ15534211-2049282		iPCy	-87.78	23.79	0.99	304.57	276.14
2MASSJ15583692-2257153	M	PCy	11.34	-80.22	1.79	589.50	534.48
2MASSJ16001844-2230114	M	PCy	45.14	-274.83	0.98	279.34	253.27
2MASSJ16035767-2031055		PCy	11.78	-69.55	1.33	510.01	462.41
2MASSJ16035793-1942108		DA		14.11	0.87	428.31	388.34
				144.62			
2MASSJ16041740-1942287		Combo	71.3	-12.68	0.95	352.99	320.04
				150.68			
2MASSJ16041893-2430392		Combo	48.95	-9.45	1.77	282.67	256.29
				157.44			
2MASSJ15354856-2958551_E		iPCy	-11.78	106.82	1.03	272.08	246.69

2MASSJ15354856-2958551_W		iPCy	-0.33	126.56	1.03	272.08	246.69
2MASSJ15514032-2146103	M	Abs		49.37	0.73	315.37	285.93
2MASSJ15530132-2114135		iPCy	-55.62	118.21	0.73	315.37	285.93
2MASSJ15582981-2310077	M	Combo	-27.6	-100.0	0.73	315.37	285.93
				101.87			
2MASSJ16014086-2258103	M	LVA	-10.73	-27.51	0.99	345.39	313.15
2MASSJ16020757-2257467		Combo	35.15	-44.86	0.79	460.95	417.92
				137.56			
2MASSJ16024152-2138245		Combo	-6.25	-124.45	0.62	272.31	246.89
				124.24			
2MASSJ16054540-2023088		Combo	1.66	-34.35	1.03	272.08	246.69
				124.78			
2MASSJ16062196-1928445		Combo	34.11	-73.48	1.42	351.83	318.99
				191.51			
2MASSJ16063539-2516510	M	iPCy	-78.39	-5.61	0.56	348.77	316.22
2MASSJ16064385-1908056		DA		-78.86	1.09	535.63	485.64
				118.42			
2MASSJ16072625-2432079		iPCy	-56.43	70.64	1.25	297.81	270.01
2MASSJ16081566-2222199		PCy	48.59	-8.53	1.00	395.08	358.21
2MASSJ16082324-1930009	M	LVA	-27.51	13.66	1.33	414.53	375.84
2MASSJ16082751-1949047	M	iPCy	-64.12	0.0	0.87	247.33	224.25
2MASSJ16090002-1908368		iPCy	-43.78	115.16	0.73	315.37	285.93
2MASSJ16090075-1908526	M	iPCy	-57.09	50.0	1.35	411.62	373.20
2MASSJ16095361-1754474	M	iPCy	-72.74	126.61	0.56	348.77	316.22
2MASSJ16104636-1840598		Combo	27.89	-67.28	0.65	333.46	302.34
				114.3			
2MASSJ16111330-2019029		Combo	-23.26	-177.56	0.52	445.84	404.23
				123.46			
2MASSJ16123916-1859284	M	PCy	0.0	-62.801	1.19	400.18	362.83
2MASSJ16133650-2503473	M	LVA	-13.8	-30.13	0.95	358.63	325.16
2MASSJ16135434-2320342	M	Combo	-12.73	-25.74	1.13	259.96	235.69
				136.06			
2MASSJ16141107-2305362		Abs		-48.91	1.62	542.01	491.42
2MASSJ16143367-1900133		Combo	-38.24	-137.23	2.10	229.36	207.96
				68.81			
2MASSJ16154416-1921171	M	iPCy	-115.87	59.07	1.21	504.34	457.27
2MASSJ16181904-2028479	M	iPCy	-80.19	-18.31	0.84	270.03	244.82

**Notes.** An 'M' in column 2 is spectra that was fit using manually defined initial guesses

## Appendix A: Tables of source information

Table A.1: Stellar and accretion properties for the targets in the Lupus region from Frasca et al. (2017); Alcalá et al. (2019).

Object	dist [pc]	SpT	$A_V$ [mag.]	$i_{disk}$ [°]	$L_*$ [ $L_\odot$ ]	$\log L_{acc}$	$M_*$ [ $M_\odot$ ]	$\log \dot{M}_{acc}$	Notes
Sz66	157	M3	1.00	69.0	0.22	-1.76	0.29	-8.50	LVC
AKC2006-19	153	M5	0.00	60.0	0.02	-4.08	0.14	-10.97	
Sz69	155	M4.5	0.00	43.53	0.09	-2.77	0.20	-9.48	LVC, HVC
Sz71	156	M1.5	0.50	40.82	0.33	-2.17	0.41	-9.02	LVC
Sz72	156	M2	0.75	75.0	0.27	-1.77	0.37	-8.60	LVC, HVC
Sz73	157	K7	3.50	49.76	0.46	-0.96	0.78	-8.12	LVC, HVC
Sz74	159	M3.5	1.50		1.16	-1.45	0.30	-7.81	LVC
Sz83	160	K7	0.00	18.0	1.49	-0.25	0.67	-7.08	
Sz84	153	M5	0.00	73.99	0.13	-2.68	0.17	-9.23	td, LVC
Sz130	160	M2	0.00	55.0	0.18	-2.14	0.39	-9.09	LVC, HVC
Sz88A	158	M0	0.25	50.0	0.31	-1.40	0.61	-8.49	LVC
Sz88B	159	M4.5	0.00	50.0	0.07	-3.30	0.20	-10.05	LVC
Sz91	159	M1	1.20	48.0	0.20	-2.00	0.51	-9.07	td, LVC
Lup713	174	M5.5	0.00		0.02	-3.62	0.11	-10.40	
Lup604s	160	M5.5	0.00	0.0	0.04	-3.89	0.12	-10.56	LVC
Sz97	158	M4	0.00	0.0	0.11	-3.11	0.24	-9.88	LVC
Sz99	159	M4	0.00		0.05	-2.80	0.23	-9.73	LVC, HVC
Sz100	137	M5.5	0.00	45.11	0.08	-3.33	0.14	-9.87	td, LVC, HVC
Sz103	160	M4	0.70	50.0	0.12	-2.60	0.23	-9.33	LVC, HVC
Sz104	166	M5	0.00	0.0	0.07	-3.36	0.16	-10.03	LVC
Lup706	159	M7.5	0.00		0.002	-5.00	0.06	-11.90	sl
Sz106	162	M0.5	1.00		0.06	-2.68	0.57	-10.07	sl, LVC
Par-Lup3-3	159	M4	2.20	0.0	0.15	-3.10	0.23	-9.77	
Par-Lup3-4	151	M4.5	0.00		0.002	-4.35	0.17	-11.81	sl, LVC
Sz110	160	M4	0.00	63.0	0.18	-2.20	0.23	-8.84	LVC
Sz111	158	M1	0.00	55.0	0.21	-2.40	0.51	-9.47	td, LVC
Sz112	160	M5	0.00	0.0	0.12	-3.39	0.17	-9.94	td, LVC
Sz113	163	M4.5	1.00	10.78	0.04	-2.28	0.19	-9.12	LVC, HVC
2MASSJ16085953-3856275	150	M8.5	0.00		0.01	-4.85	0.02	-11.02	LVC
SSTc2d160901.4-392512	164	M4	0.50	60.0	0.10	-3.17	0.23	-9.95	LVC
Sz114	162	M4.8	0.30	15.84	0.21	-2.68	0.19	-9.17	LVC, HVC
Sz115	158	M4.5	0.50		0.11	-2.91	0.20	-9.57	
Lup818s	157	M6	0.00	0.0	0.02	-4.31	0.08	-10.96	LVC
Sz123A	159	M1	1.25	40.0	0.13	-2.00	0.55	-9.21	td, LVC, HVC
Sz123B	159	M2	0.00	40.0	0.03	-2.90	0.40	-10.24	sl, LVC, HVC
SST-Lup3-1	165	M5	0.00	73.0	0.04	-3.77	0.16	-10.53	
Sz65	155	K7	0.60	61.46	0.89	-2.57	0.70	-9.52	
AKC2006-18	139	M6.5	0.00	60.0	0.01	-4.60	0.07	-11.23	LVC
SSTc2dJ154508.9-341734	155	M5.5	5.50	47.0	0.06	-1.77	0.14	-8.36	LVC, HVC
Sz68	154	K2	1.00	32.89	5.42	-1.18	2.15	-8.39	
SSTc2dJ154518.5-342125	152	M6.5	0.00	25.8	0.04	-4.29	0.08	-10.72	LVC, HVC
Sz81A	160	M4.5	0.00	0.0	0.25	-2.44	0.19	-8.92	LVC
Sz81B	160	M5.5	0.00	0.0	0.12	-3.14	0.15	-9.61	LVC
Sz129	162	K7	0.90	31.74	0.43	-1.13	0.78	-8.30	LVC
SSTc2dJ155925.2-423507	147	M5	0.00		0.02	-4.42	0.14	-11.29	LVC
RY Lup	159	K2	0.40	55.0	1.87	-0.85	1.53	-8.16	td, LVC
SSTc2dJ160000.6-422158	161	M4.5	0.00	0.0	0.10	-3.04	0.20	-9.73	LVC
SSTc2dJ160002.4-422216	164	M4	1.40	66.0	0.18	-2.92	0.23	-9.56	
SSTc2dJ160026.1-415356	164	M5.5	0.90		0.08	-3.22	0.14	-9.76	
MY Lup	157	K0	1.30	72.98	0.85	-0.65	1.09	-8.01	td
Sz131	160	M3	1.30	59.0	0.15	-2.34	0.30	-9.18	LVC, HVC
Sz133	153	K5	1.80	78.53	0.07	-1.78			sl, bz, LVC
SSTc2dJ160703.9-391112	159	M4.5	0.60	61.0	0.003	-5.40	0.16	-12.76	sl, td?, LVC
Sz90	160	K7	1.80	61.31	0.42	-1.79	0.78	-8.96	LVC, HVC
Sz95	158	M3	0.80	50.0	0.26	-2.70	0.29	-9.40	
Sz96	157	M1	0.80	50.0	0.42	-2.51	0.45	-9.37	LVC
2MASSJ16081497-3857145	159	M5.5	1.50	75.0	0.01	-3.60	0.10	-10.60	LVC



Sz98	156	K7	1.00	47.10	1.53	-0.71	0.67	-7.54	LVC, HVC
Lup607	175	M6.5	0.00	0.0	0.05	-5.02	0.09	-11.60	LVC
Sz102	159	K2	0.70	57.60	0.01	-2.20			sl, bz, LVC, HVC
SSTc2dJ160830.7-382827	156	K2	0.20	73.0	1.84	-2.02	1.53	-9.32	td, LVC
SSTc2dJ160836.2-392302	154	K6m	1.70	56.2	1.15	-1.03	0.83	-8.04	td?, LVC, HVC
Sz108B	169	M5	1.60	49.09	0.11	-3.05	0.17	-9.62	LVC, HVC
2MASSJ16085324-3914401	168	M3	1.90	60.72	0.21	-3.25	0.29	-10.00	
2MASSJ16085373-3914367	159	M5.5	4.00		0.00	-3.90	0.10	-10.94	
2MASSJ16085529-3848481	158	M6.5	0.00	0.0	0.05	-4.31	0.09	-10.72	LVC, HVC
SSTc2dJ160927.0-383628	159	M4.5	2.20	51.0	0.07	-1.50	0.20	-8.25	LVC, HVC
Sz117	159	M3.5	0.50	0.0	0.28	-2.30	0.25	-8.91	LVC, HVC
Sz118	164	K5	1.90	67.0	0.72	-1.97	1.04	-9.21	LVC
2MASSJ16100133-3906449	193	M6.5	1.70	35.0	0.19	-3.43	0.14	-9.74	LVC
SSTc2dJ161018.6-383613	159	M5	0.50		0.04	-4.00	0.15	-10.76	
SSTc2dJ161019.8-383607	159	M6.5	0.00	55.0	0.04	-4.10	0.08	-10.52	
SSTc2dJ161029.6-392215	163	M4.5	0.90	66.54	0.11	-3.38	0.20	-10.05	td, LVC
SSTc2dJ161243.8-381503	160	M1	0.80	43.69	0.39	-2.19	0.45	-9.07	LVC
SSTc2dJ161344.1-373646	160	M5	0.60	0.0	0.04	-2.49	0.16	-9.24	LVC, HVC
Sz75/GQ Lup	152	K6	0.70	60.60	1.48	-0.69	0.80	-7.63	LVC
Sz76	160	M4	0.20	38.9	0.18	-2.55	0.23	-9.18	td, LVC
Sz77	155	K7	0.00	61.70	0.59	-1.67	0.75	-8.76	
RXJ1556.1-3655	158	M1	1.00	49.4	0.26	-0.85	0.49	-7.85	LVC
Sz82/IM Lup	159	K5	0.90	48.40	2.60	-1.05	0.95	-7.98	td
EX Lup	158	M0	1.10	30.80	0.76	-0.91	0.53	-7.74	

**Notes.** Disk inclinations from Tazzari et al. (2017); Ansdell et al. (2018); Yen et al. (2018). Information on the presence of winds or jets is from optical emission lines analysed in Natta et al. (2014) and Nisini et al. (2018)

td : YSO with transitional disk ; sl : sub-luminous YSO; bz : sub-luminous object falling below the zero-age main-sequence on the HR diagram

Table A.2: Stellar and accretion properties for the targets in the Upper Scorpius region from Manara et al. (2020).

Object	dist [pc]	SpT	$A_V$ [mag.]	$i_{disk}$ [°]	$L_*$ [ $L_\odot$ ]	$\log L_{acc}$	$M_*$ [ $M_\odot$ ]	$\log \dot{M}_{acc}$	Notes
2MASSJ15534211-2049282	136 ± 4	M4	1.2	89.0	0.09	-2.6	0.24	3.66·10 <sup>-10</sup>	f
2MASSJ15583692-2257153	166 ± 4	K0	0.0		2.57	-0.5	1.63*	1.59·10 <sup>-08</sup>	f
2MASSJ16001844-2230114	138 ± 9	M4.5	0.8	45.0	0.08	-1.9	0.20	2.03·10 <sup>-09</sup>	f
2MASSJ16035767-2031055	143 ± 1	K6	0.7	69.0	0.48	-1.8	0.91	8.81·10 <sup>-10</sup>	f
2MASSJ16035793-1942108	158 ± 2	M2	0.3	56.0	0.13	-5.1	0.42	6.69·10 <sup>-13</sup>	f
2MASSJ16041740-1942287	161 ± 2	M3	0.7	80.0	0.14	-4.3	0.31	6.04·10 <sup>-12</sup>	f
2MASSJ16041893-2430392	145	M2	0.3		0.45	-3.1	0.37	1.48·10 <sup>-10</sup>	
2MASSJ16042165-2130284	150 ± 1	K3	1.4		0.90	-3.2	1.24	3.09·10 <sup>-11</sup>	td
2MASSJ15354856-2958551_E	145	M4.5	0.0	46.0	0.10	-2.8	0.20	3.53·10 <sup>-10</sup>	f,b
2MASSJ15354856-2958551_W	145	M4.5	0.0	46.0	0.10	-2.9	0.20	2.73·10 <sup>-10</sup>	b
2MASSJ15514032-2146103	142 ± 2	M4.5	0.3	83.0	0.05	-3.5	0.19	5.01·10 <sup>-11</sup>	e
2MASSJ15530132-2114135	146 ± 2	M4.5	0.8	47.0	0.05	-3.0	0.19	1.52·10 <sup>-10</sup>	f
2MASSJ15582981-2310077	147 ± 3	M4.5	1.0	32.0	0.05	-2.3	0.19	7.16·10 <sup>-10</sup>	f
2MASSJ16014086-2258103	145	M3	1.2	74.0	0.12	-1.2	0.31	7.42·10 <sup>-09</sup>	f
2MASSJ16020757-2257467	140 ± 1	M2	0.4	57.0	0.08	-3.8	0.44	1.08·10 <sup>-11</sup>	f
2MASSJ16024152-2138245	142 ± 2	M5.5	0.6	41.0	0.03	-2.9	0.12	2.76·10 <sup>-10</sup>	f
2MASSJ16054540-2023088	145 ± 2	M4.5	0.6	67.0	0.10	-2.8	0.20	3.58·10 <sup>-10</sup>	f
2MASSJ16062196-1928445	145	M1	0.8	85.0	0.34	-1.3	0.46	6.13·10 <sup>-09</sup>	td
2MASSJ16063539-2516510	139 ± 3	M4.5	0.0	74.0	0.03	-5.1	0.18	8.62·10 <sup>-13</sup>	e
2MASSJ16064385-1908056	144 ± 7	K7	0.4	48.0	0.29	-2.3	0.82	2.65·10 <sup>-10</sup>	e
2MASSJ16072625-2432079	143 ± 2	M3	0.7	43.0	0.18	-2.6	0.29	4.56·10 <sup>-10</sup>	f
2MASSJ16081566-2222199	140 ± 2	M2	0.5	86.0	0.15	-3.7	0.41	1.99·10 <sup>-11</sup>	f
2MASSJ16082324-1930009	138 ± 1	M0	1.1	74.0	0.32	-2.0	0.61	7.90·10 <sup>-10</sup>	f
2MASSJ16082751-1949047	145	M5.5	0.6	41.0	0.06	-3.1	0.14	1.97·10 <sup>-10</sup>	e
2MASSJ16090002-1908368	139 ± 3	M4.5	0.3	63.0	0.05	-4.2	0.19	1.02·10 <sup>-11</sup>	f
2MASSJ16090075-1908526	138 ± 1	M0	1.0	56.0	0.32	-1.7	0.60	1.74·10 <sup>-09</sup>	f
2MASSJ16095361-1754474	158 ± 5	M4.5	0.5	86.0	0.04	-4.5	0.18	4.54·10 <sup>-12</sup>	f
2MASSJ16104636-1840598	143 ± 3	M4.5	1.2	71.0	0.04	-3.9	0.19	1.45·10 <sup>-11</sup>	f
2MASSJ16111330-2019029	155 ± 1	M3.5	0.6	17.0	0.03	-1.9	0.27	9.77·10 <sup>-10</sup>	f
2MASSJ16123916-1859284	139 ± 2	M1	0.6	51.0	0.22	-2.3	0.50	4.75·10 <sup>-10</sup>	f

2MASSJ16133650-2503473	145	M3	1.0	86.0	0.11	-1.6	0.32	$2.93 \cdot 10^{-09}$	f
2MASSJ16135434-2320342	145	M4.5	0.3	52.0	0.12	-2.3	0.20	$1.18 \cdot 10^{-09}$	f
2MASSJ16141107-2305362	145	K4	0.3	4.0	1.05	-1.4	1.25	$2.09 \cdot 10^{-09}$	f
2MASSJ16143367-1900133	$142 \pm 2$	M3	1.9	69.0	0.52	-2.7	0.29	$5.17 \cdot 10^{-10}$	f
2MASSJ16154416-1921171	$132 \pm 2$	K7	2.8	40.0	0.30	-0.3	0.81	$2.44 \cdot 10^{-08}$	f
2MASSJ16181904-2028479	$138 \pm 2$	M5	1.6	56.0	0.05	-3.4	0.16	$8.05 \cdot 10^{-11}$	e

**Notes.** Disk inclinations from Barenfeld et al. (2017). Disk types from Barenfeld et al. (2016); Luhman & Mamajek (2012); Carpenter et al. (2006) f: full disk; td: transitional disk; e: evolved disk; b: binary source

## Appendix B: Aligning the NIR and VIS spectra

During the data reduction, aligning the wavelength axis of both the NIR and VIS spectra is a crucial step to ensure the correct velocities are measured in the He I  $\lambda 10830$  Å line. We examined the Pa $\delta$  1004.94 nm and the Li 670.78 nm lines to measure the velocity correction needed for this alignment. First, the radial velocity and heliocentric velocity corrections are applied to the spectra. We then fit the Li line with a 1D Gaussian to measure any shift from its rest wavelength of 670.78 nm. Both the NIR and VIS spectra are shifted so the Li line in the VIS spectra is centred at  $0 \text{ km s}^{-1}$ . The majority of our sample (109 sources in total consisting of 73 sources in Lupus, and 36 in Upper Sco) used the velocity shift measured by the Gaussian fits. In nine spectra (all in Lupus), the median Li shift of  $-0.5 \text{ km s}^{-1}$  is applied to the spectra. In these cases, the Li line is either not detected or the signal-to-noise is too low to properly fit with a Gaussian.

Next, the Pa $\delta$  1004.94 nm line, in both the NIR and VIS spectra, is fitted using a 1D Gaussian. The velocity difference between the peak of the Pa $\delta$  lines in the NIR and VIS spectra is used to shift the NIR arm, to be aligned with the VIS arm. For the majority of our spectra, the NIR and VIS arms were already well-aligned, so a total of 73 sources (54 in Lupus and 19 in Upper Sco) are not shifted based on the Pa $\delta$  line. In 45 sources (28 in Lupus, 17 in Upper Sco), the velocity correction found with the Pa $\delta$  line is applied to align the NIR and VIS spectra. However, in eight (seven in Lupus, one in Upper Sco) of these sources the Pa $\delta$  shift measured with the Gaussian fit was too large ( $> \pm 20 \text{ km s}^{-1}$ ), and was not appropriate for aligning the spectra. This is due to a low signal-to-noise ratio in the Pa $\delta$  line for these sources. In these cases, the median value of the non-zero Pa $\delta$  shifts was used - this is  $9 \text{ km s}^{-1}$  in Lupus, and  $-2.9 \text{ km s}^{-1}$  in Upper Sco.

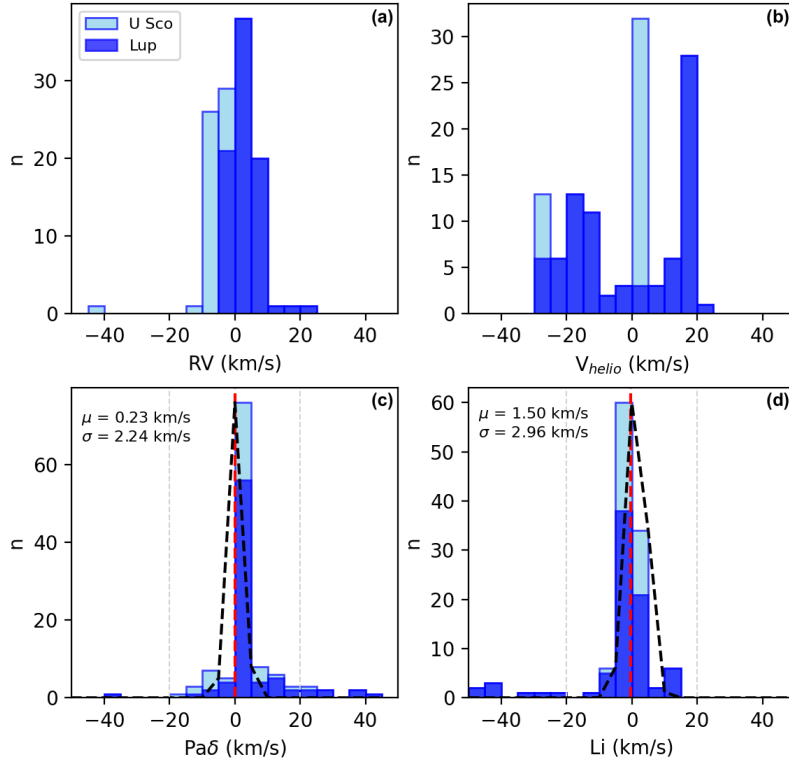


**Fig. B.1:** Histograms of the velocity corrections applied to the spectra for sources in both star forming regions. Panels (a) and (b) show the radial velocity and the heliocentric velocity corrections. Panels (c) and (d) show the velocity corrections measured from the Pa $\delta$  and Li lines. The red dashed line marks the median value of the Pa $\delta$  and Li shifts, with the corresponding mean and standard deviation listed in each panel.

In Figure B.1, we plot histograms of all velocity corrections applied to our spectra in both star forming regions. In each panel, dark blue bars represent sources in Lupus, while light blue shows the Upper Sco sources. Panels (a) and (b) show the radial velocity

and the heliocentric velocity corrections. Panels (c) and (d) show the velocity corrections measured from the Pa $\delta$  and Li lines. The red dashed line marks the median value of the Pa $\delta$  and Li shifts, with the corresponding mean and standard deviation listed in each panel. Vertical dashed lines in panels (c) and (d) mark the velocities above which we use the median velocity shifts listed above. We find the standard deviations for both the Li line and Pa $\delta$  line velocity corrections,  $\sigma$ , to be less than  $3 \text{ km s}^{-1}$  ( $2.96 \text{ km s}^{-1}$  in the Li line velocity shifts and  $2.24 \text{ km s}^{-1}$  for the Pa $\delta$  line). Adding these in quadrature, the combined error due to the velocity corrections is  $3.7 \text{ km s}^{-1}$  and thus do not introduce large uncertainties in the observed maximum velocities in the He I  $\lambda 10830 \text{ \AA}$  line (see Section 4). Also, since  $3\sigma$  is less than the velocity resolution (of  $\approx 11 \text{ km s}^{-1}$  and  $16 \text{ km s}^{-1}$  for the VIS and NIR arms, respectively), these velocity shifts are not likely to affect the number of each profile type observed in the sample.

### Appendix C: He I $\lambda 10830 \text{ \AA}$ profiles in the Lupus sample

We present He I  $\lambda 10830 \text{ \AA}$  profiles of the Lupus sample arranged by the fitted profile types in Figures C.1 & C.2. The profiles are normalised to the continuum level and rescaled between  $\pm 1$  for plotting. We mark two photospheric absorption features (i.e Si I  $10830.1 \text{ \AA}$  and Na I  $10837.8 \text{ \AA}$ , at  $-88 \text{ km s}^{-1}$  and  $+126 \text{ km s}^{-1}$ , respectively) on the each plot, as these may contribute to the observed He I  $\lambda 10830 \text{ \AA}$  absorption features.

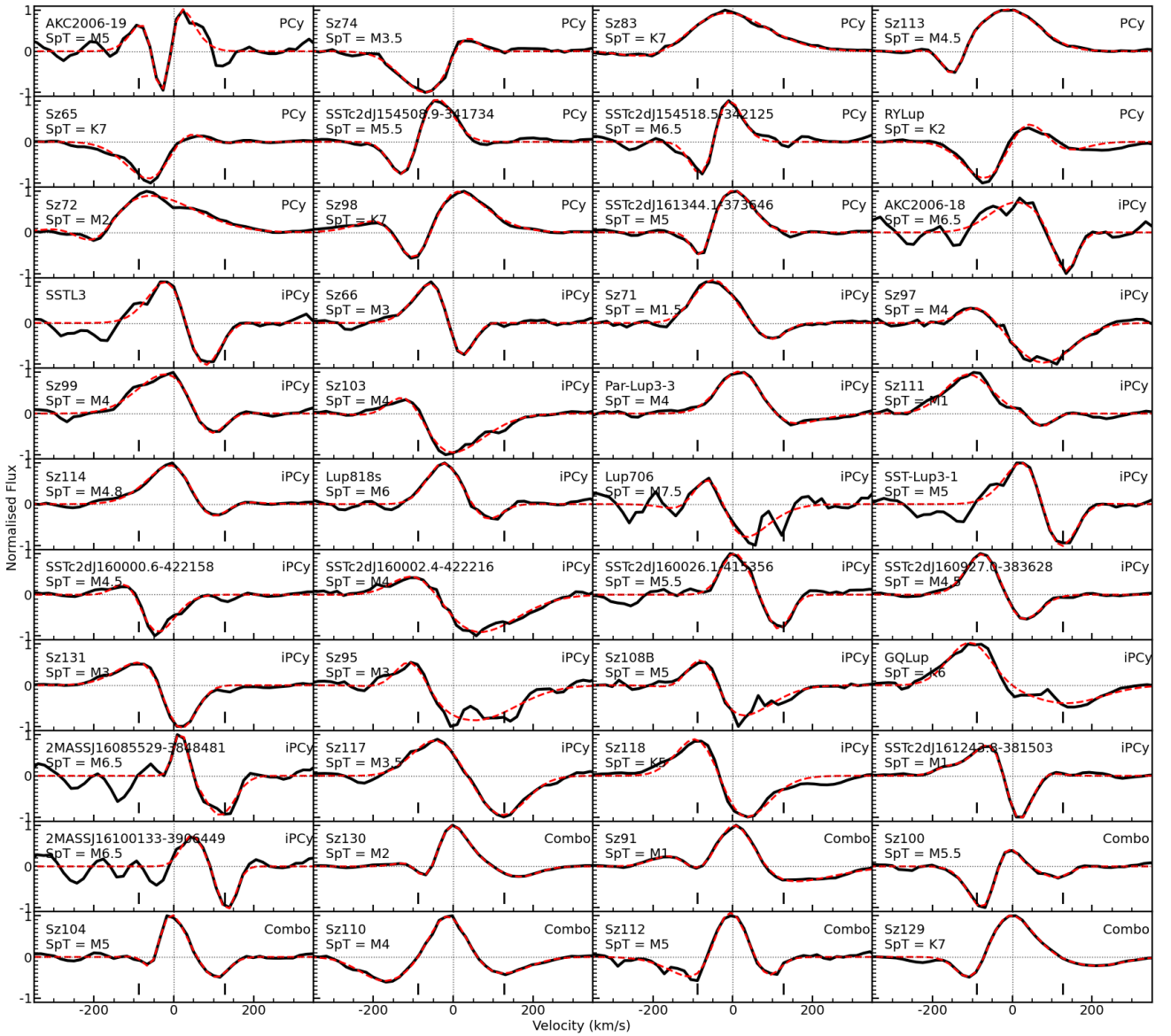


Fig. C.1: He I  $\lambda 10830 \text{ \AA}$  profiles of the Lupus sample, grouped by profile type. The profiles are normalised to the continuum level and rescaled between  $\pm 1$  for plotting. The black vertical dashes (at  $-88 \text{ km s}^{-1}$  and  $+126 \text{ km s}^{-1}$ ) mark photospheric absorption features (i.e Si I  $10830.1 \text{ \AA}$  and Na I  $10837.8 \text{ \AA}$ )

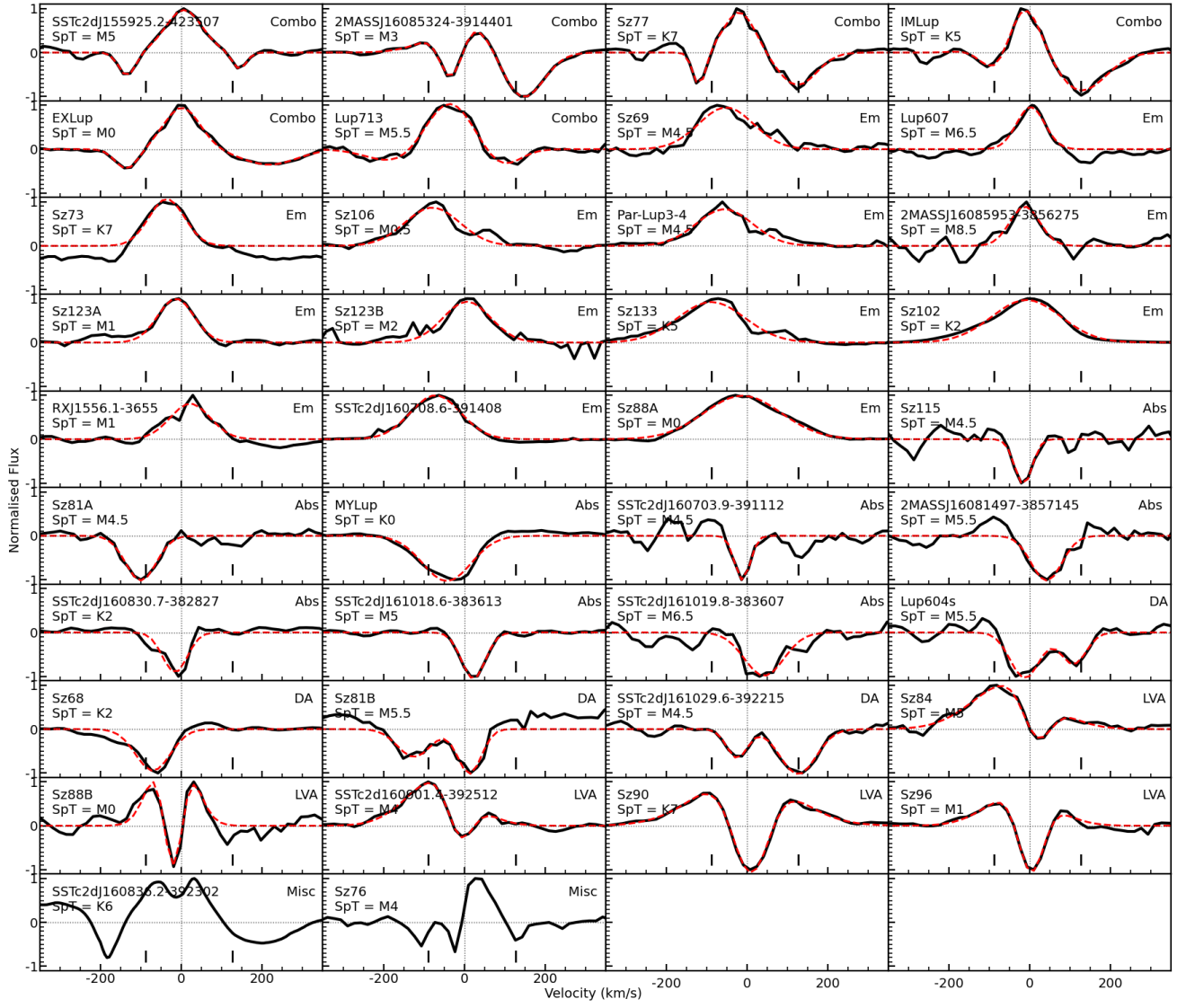


Fig. C.2: He I  $\lambda 10830$  Å profiles of the Lupus sample, grouped by profile type. The profiles are normalised to the continuum level and rescaled between  $\pm 1$  for plotting. The black vertical dashes (at  $-88 \text{ km s}^{-1}$  and  $+126 \text{ km s}^{-1}$ ) mark photospheric absorption features (i.e Si I  $10830.1 \text{ Å}$  and Na I  $10837.8 \text{ Å}$ )

## Appendix D: He I $\lambda 10830$ Å profiles in the Upper Scorpius sample

We present He I  $\lambda 10830$  Å profiles of the Upper Scorpius sample arranged by the fitted profile types in Figure D.1. The profiles are normalised to the continuum level and rescaled between  $\pm 1$  for plotting. We mark two photospheric absorption features (i.e Si I 10830.1 Å and Na I 10837.8 Å, at  $-88$  km s $^{-1}$  and  $+126$  km s $^{-1}$ , respectively) on the each plot, as these may contribute to the observed He I  $\lambda 10830$  Å absorption features.

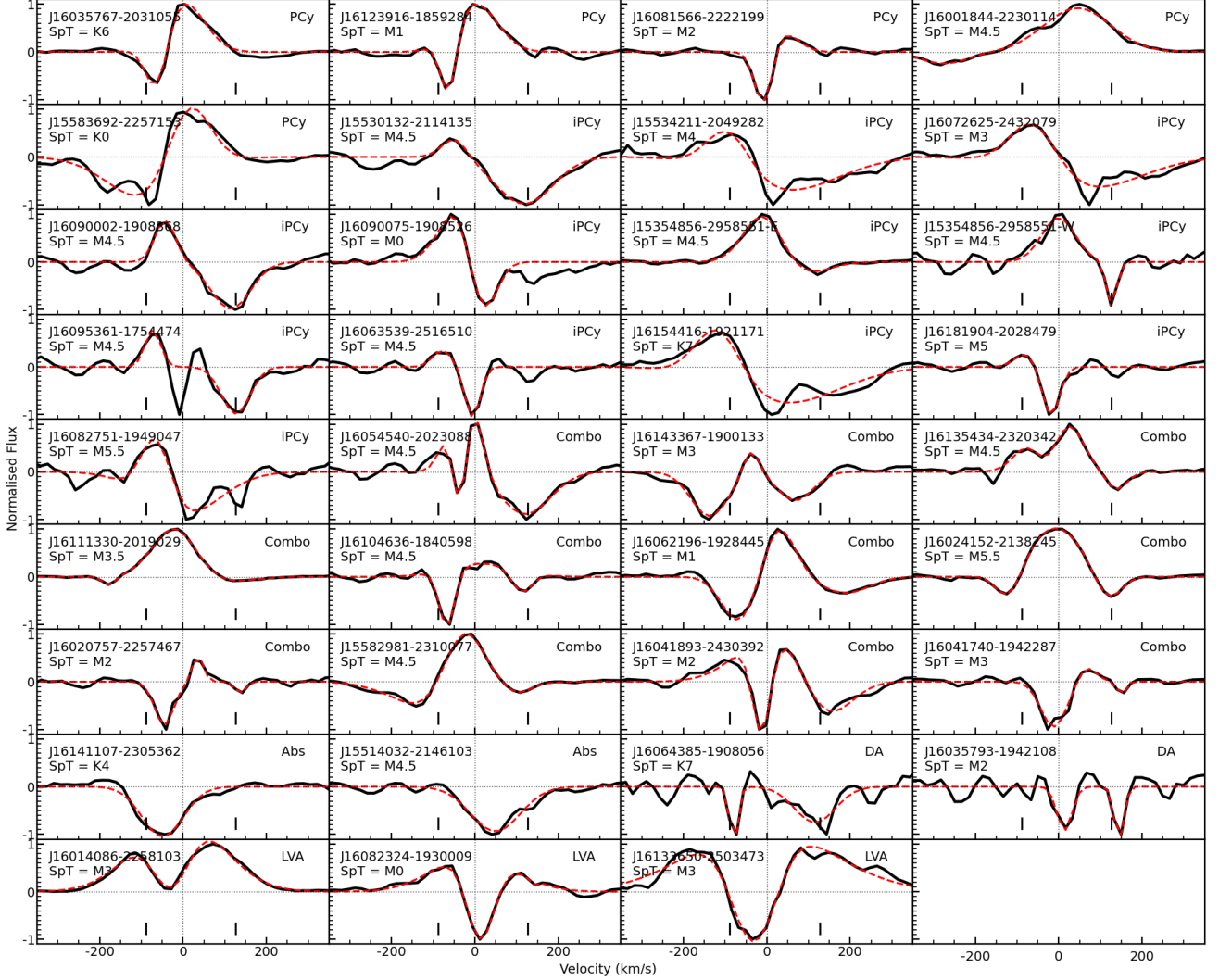


Fig. D.1: He I  $\lambda 10830$  Å profiles of the Upper Scorpius sample, grouped by profile type. The profiles are normalised to the continuum level and rescaled between  $\pm 1$  for plotting. The black vertical dashes (at  $-88$  km s $^{-1}$  and  $+126$  km s $^{-1}$ ) mark photospheric absorption features (i.e Si I 10830.1 Å and Na I 10837.8 Å)



## Appendix E: He I $\lambda 10830$ Å profiles in Class III sources

43 Class III spectra, from Manara et al. (2013,2017), are plotted centred on the He I  $\lambda 10830$  Å line over a velocity interval of  $\pm 350$  km s<sup>-1</sup>. The subplots are arranged by spectral type (noted on each panel in Figure E.1). Each spectrum was normalized to the continuum level by taking the mean continuum level on either side of the He I line. All spectra are corrected for the radial and heliocentric velocities. The grey vertical line marks 0 km/s. The black vertical dashes (at -88 km s<sup>-1</sup> and +126 km s<sup>-1</sup>) mark strong photospheric absorption features (i.e Si I 10830.1 Å and Na I 10837.8 Å) which are particularly strong in SpTs G and K. For K-type SpT there also appears to be a persistent absorption feature centred on 0 km/s. Generally, little to no emission is seen for these sources. Strong and broad absorption centred on 0 km/s is seen in only two sources (Sz107 and RXJ0445.8+1556).

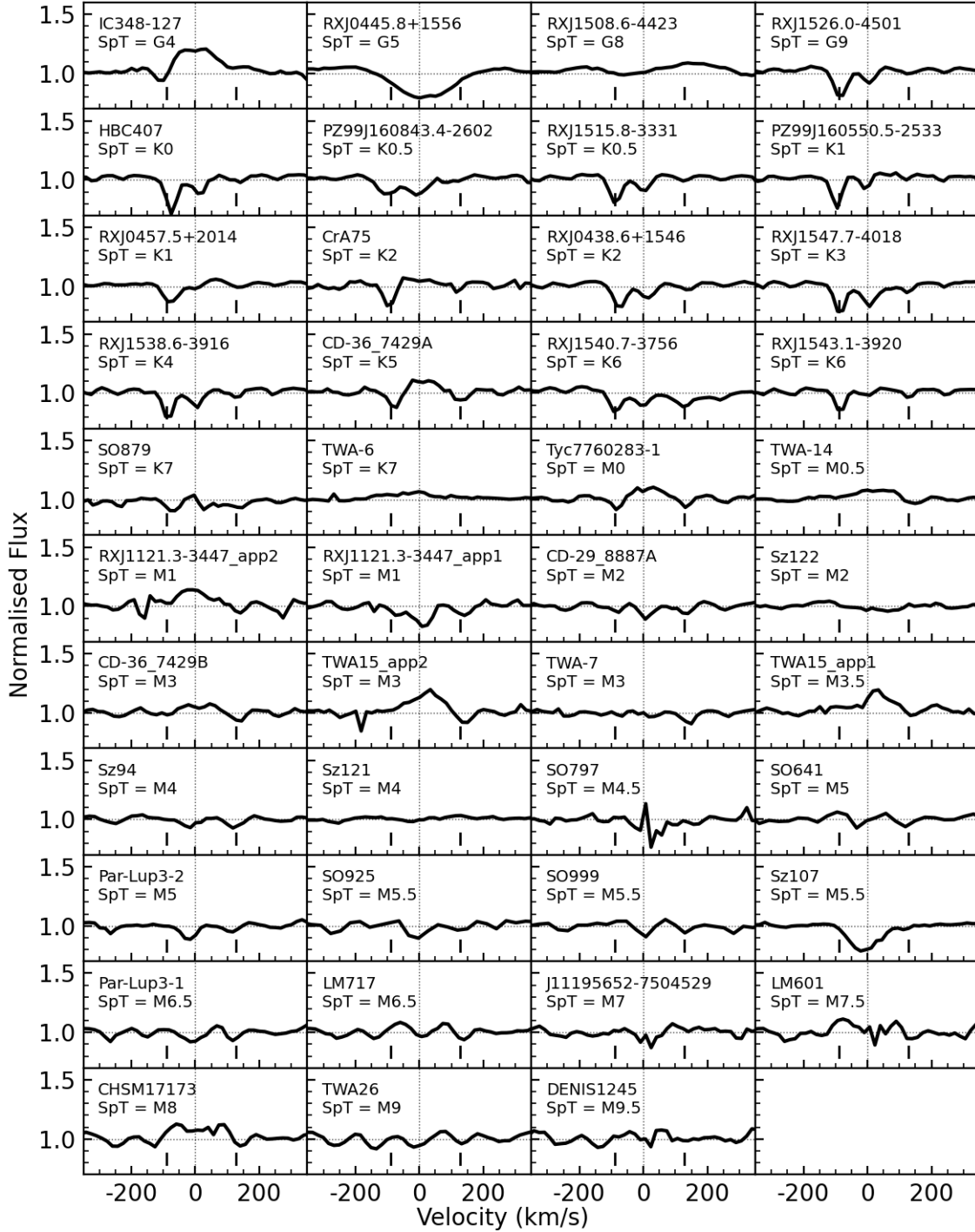


Fig. E.1: He I  $\lambda 10830$  Å profiles for a sample of 43 Class III sources. We do not observe absorption nor emission features suitable for classifying the profiles as in Section 3.2. The black vertical dashes (at -88 km s<sup>-1</sup> and +126 km s<sup>-1</sup>) mark photospheric absorption features (i.e Si I 10830.1 Å and Na I 10837.8 Å)